Comparison of Radiative Energy Flows in Observational Datasets and Climate Modeling

EHRHARD RASCHKE

Max Planck Institute for Meteorology and University of Hamburg, Hamburg, Germany

STEFAN KINNE

Max Planck Institute for Meteorology, Hamburg, Germany

WILLIAM B. ROSSOW

NOAA–Cooperative Remote Sensing Science and Technology, The City College of New York, New York, New York

PAUL W. STACKHOUSE JR.

NASA Langley Research Center, Hampton, Virginia

MARTIN WILD

Institute for Atmospheric and Climate Studies, ETH Zürich, Zurich, Switzerland

(Manuscript received 28 October 2014, in final form 3 October 2015)

ABSTRACT

This study examines radiative flux distributions and local spread of values from three major observational datasets (CERES, ISCCP, and SRB) and compares them with results from climate modeling (CMIP3). Examinations of the spread and differences also differentiate among contributions from cloudy and clear-sky conditions. The spread among observational datasets is in large part caused by noncloud ancillary data. Average differences of at least $10\,\mathrm{W\,m^{-2}}$ each for clear-sky downward solar, upward solar, and upward infrared fluxes at the surface demonstrate via spatial difference patterns major differences in assumptions for atmospheric aerosol, solar surface albedo and surface temperature, and/or emittance in observational datasets. At the top of the atmosphere (TOA), observational datasets are less influenced by the ancillary data errors than at the surface. Comparisons of spatial radiative flux distributions at the TOA between observations and climate modeling indicate large deficiencies in the strength and distribution of model-simulated cloud radiative effects. Differences are largest for lower-altitude clouds over low-latitude oceans. Global modeling simulates stronger cloud radiative effects (CRE) by $+30\,\mathrm{W\,m^{-2}}$ over trade wind cumulus regions, yet smaller CRE by about $-30\,\mathrm{W\,m^{-2}}$ over (smaller in area) stratocumulus regions. At the surface, climate modeling simulates on average about $15\,\mathrm{W\,m^{-2}}$ smaller radiative net flux imbalances, as if climate modeling underestimates latent heat release (and precipitation). Relative to observational datasets, simulated surface net fluxes are particularly lower over oceanic trade wind regions (where global modeling tends to overestimate the radiative impact of clouds). Still, with the uncertainty in noncloud ancillary data, observational data do not establish a reliable reference.

1. Introduction

Early attempts to measure the radiation budget components of Earth from space began more than five decades ago with simple wide-field-of-view sensors on the *Explorer 7* satellite. Since then our understanding of radiative energy flows has advanced greatly with the help of more capable narrow-field-of-view satellite sensors, as illustrated in Fig. 1.

Scanning radiometers, now offering more detailed spatial information, were first flown on single satellites of the TIROS, Nimbus, and COSMOS series (House et al. 1986). Next, the multisatellite project ERBE (Barkstrom 1984) provided measurements from up to three satellites between 1985 and 1990. Continuous

Corresponding author address: Ehrhard Raschke, Max Planck Institute for Meteorology and University of Hamburg, Bundesstrasse 53, 20146 Hamburg, Germany.
E-mail: ehrhard.raschke@mpimet.mpg.de

DOI: 10.1175/JAMC-D-14-0281.1

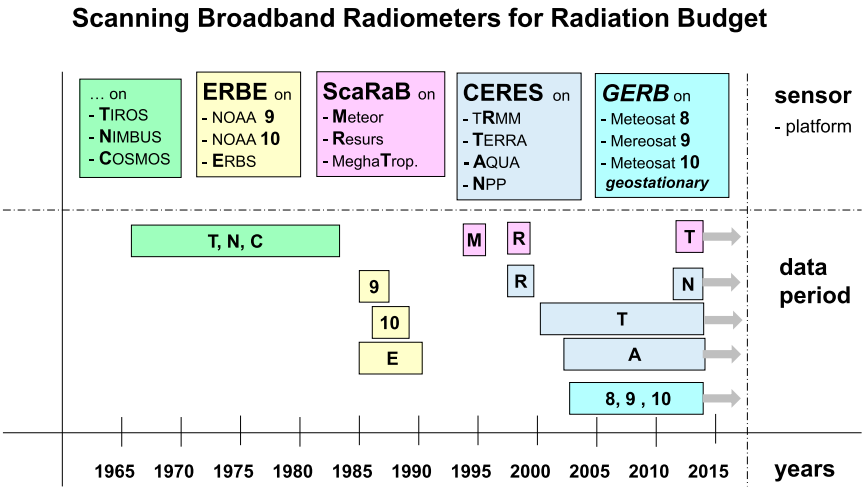

FIG. 1. History of scanning satellite sensors used to measure the broadband SW and LW radiation leaving the Earth–atmosphere system to space. Measurements by ScaRaB, CERES, and GERB instruments are ongoing (as designated by arrows).

measurements began in 2000 with the Clouds and Earth's Radiant Energy System (CERES) radiometers (Wielicki et al. 1995; Loeb et al. 2009) on two satellites from 2002 and continues today. In addition, the French–Soviet–German Scanner for Radiation Budget experiment (ScaRaB; Duvel et al. 2001) provided intermittent coverage for several months in 1995 and 1999 and has provided data since 2012 from the near-equatorial satellite *Megha-Tropiques*. Regionally limited but high temporal resolution data have been obtained by the Geostationary Earth Radiation Budget instrument (GERB; Harries et al. 2005) on the geostationary Meteosat platforms since 1998.

The required accuracy for atmospheric radiative fluxes depends on the spatial and temporal scales considered as well as the applications (Smith et al. 1986, 2006). Accuracy requirements range from $15\,\mathrm{W\,m^{-2}}$ for weather scales to less than $1\,\mathrm{W\,m^{-2}}$ for climate scales (Ohring et al. 2005). Direct satellite determinations of the broadband radiative fluxes at the top of the atmosphere (TOA) face uncertainties related to instrumental limitations (e.g., calibration, spectral sensitivity), subsampling in time and space, viewing geometry, and data interpretation. The determination of radiative fluxes at the surface and in the atmosphere based on satellite observations must necessarily involve many datasets describing clouds (vertical structure, temperature, optical depth, and microphysical characteristics) and other atmospheric (aerosol, water vapor, and temperature) and surface properties (albedo, temperature, and longwave emittance) that can introduce additional uncertainty (Rossow and Lacis 1990; Rossow and Schiffer 1999; Zhang et al. 1995; Wielicki et al. 1995; Kato et al. 2012). Inaccuracies and inconsistencies of these datasets can degrade the quality and usefulness of the derived radiative flux products.

The GEWEX Data Assessment Project (GDAP) set out to explore the strengths, limitations, and usefulness of satellite data records for climate applications more than a decade ago. Completed assessments have addressed precipitation (Gruber and Levizzani 2008), aerosols (Li et al. 2009), clouds (Stubenrauch et al. 2013), and most recently radiative fluxes (Raschke et al. 2012a,b).

The radiation report of the GDAP (available online at http://www.wcrp-climate.org/documents) completed an assessment effort that began a decade earlier with the collection of the then-available long-term datasets for monthly mean radiative flux spatial distributions at the TOA and surface. The data collection included an early version of the CERES (Wielicki et al. 1996; Loeb et al. 2001) products (2000–04), the International Satellite Cloud Climatology Project Flux Data (ISCCP-FD; Zhang et al. 2004) products (1984–2004), and the GEWEX Surface Radiation Budget (SRB; Gupta et al. 1999; Stackhouse et al. 2001, 2011) products (1984–2004). ISCCP and SRB, unlike CERES, do not involve direct TOA measurements of broadband radiative fluxes, but all three datasets provide radiative flux spatial distributions at the TOA and surface. All three datasets are tied to mostly independent satellite observations of clouds, aerosols, surface albedo, skin temperature, atmospheric temperature, and humidity. Thus, these datasets are referred to here as the observational datasets in contrast to climate modeling outputs, which represent simulations of clouds and the hydrological cycle.

The goal of this study is to illustrate characteristic spatial distributions of radiative fluxes from observational dataset at the TOA and surface, to quantify local uncertainty among the radiative fluxes, and to explore differences with radiative fluxes from global modeling. Characteristic observational data are defined here by the local (map grid) average of values from CERES, ISSCP, and SRB for the same 2000–03 time period, and are collectively known as the CIS dataset (CIS stands for CERES, ISCCP, and SRB). Uncertainty is estimated by the local spread (range) among the values from CERES, ISCCP, and SRB (ΔCIS). Characteristic data from global modeling are based on roughly 20 different contributions to the model comparison exercise of CMIP3. Averages between the 25th and the 75th model ensemble percentiles (locally applied) define characteristic climate modeling data (CMIP3), and differences between the 25th and the 75th ensemble percentile define the uncertainty (ΔCMIP3). Note that this uncertainty measure does not cover the entire range, as for the three observational datasets. On the other hand, the model ensemble involves output from about 20 different models.

Differences among the atmospheric radiative energy flows between the global modeling and observational data were found and investigated in the past (Wild 2008; Trenberth et al. 2011). However, many diagnosed differences have not been fully understood and still remain topics of current research (Stephens et al. 2002, 2012; Kato et al. 2013; Wild et al. 2012; L'Ecuyer et al. 2015). However, most studies argue along global annual averages, although there is additional detail offered by the spatial distribution. Thus, when exploring differences between global modeling and observational data, in this study difference maps are presented and examined,

In section 2 global and regional CIS and ΔCIS are presented at the TOA and surface, together with clear-sky fluxes and the contributions by clouds, known as the cloud radiative effect (CRE). We also explore the contributions of some particular atmospheric and surface property dataset uncertainties to ΔCIS. In section 3 the differences between (CIS and ΔCIS) and (CMIP3 and ΔCMIP3) are examined. Section 4 concludes with a summary and selected recommendations.

2. The observed CIS dataset

Three observational datasets offer radiative fluxes at the TOA and surface over multiyear time periods: CERES-geo (Edition 2D: *Terra* only; Doelling et al. 2006), ISCCP-FD (Zhang et al. 2004), and SRB (Stackhouse et al. 2001; Gupta et al. 2006). [Note that subsequent versions of the CERES and SRB datasets have been made available and are described in Loeb et al. (2009), Kato et al. (2013), and Stackhouse et al. (2011).] These fluxes are computed using a collection of observed, mostly satellite-based, datasets that describe the relevant properties of the atmosphere, including clouds, and the surface, but the TOA radiative fluxes of CERES are directly linked to satellite broadband measurements. To establish the typical features of these observational datasets, they are locally ($1° \times 1°$ latitude–longitude map grid) averaged together over a common 4-yr period (2000–03) to form the CIS dataset. In addition, the three-dataset spread, ΔCIS, is recorded to illustrate uncertainty. The contributions of clouds to averages and spread are examined based on the so-called cloud radiative effect, defined as the difference between all-sky fluxes and clear-sky (''clouds removed'') fluxes (Long and Turner 2008). Hereby, the CERES (-SRBAVG) CRE is slightly stronger than all other datasets, as its real observations tend to have lower water vapor in the clear-sky reference.

a. Ancillary data

Since the satellite data products considered here are all founded on direct inferences of cloud properties (and CERES is further based on direct inferences of TOA fluxes), we will refer to the other atmospheric (e.g., aerosol) and surface properties (e.g., albedo, temperature, emittance) information required in the calculations of radiative fluxes as ancillary data. Also there are some additional properties of clouds (particularly base location and microphysics) that are needed. Most of the ancillary data used in the observational dataset are obtained from other independent satellite retrievals or weather observation reanalyses. While their sources are usually mentioned [e.g., for ISCCP see Zhang et al. (2004) and for CERES see Loeb et al. (2009)], questions regarding their implementation and consistency remain [although see discussions in Zhang et al. (2006), (2007a), and (2010)]. To ascertain the contributions of these ancillary datasets to ΔCIS, we first diagnose the differences in the four primary ancillary datasets.

1) Solar energy input

The downward shortwave (hereinafter SW, dn) fluxes at the TOA represent the available solar energy to the Earth–atmosphere system. Analysis of the Total Irradiance Monitor (TIM) data on NASA's Solar Radiation and Climate Experiment (SORCE) mission corrected the total solar irradiance (TSI) slightly downward to $1360.8\ \mathrm{W\,m^{-2}}$ (Kopp and Lean 2011), with weak variability due to changes in the eccentricity of Earth's orbit, the position of its perihelion, the tilt (obliquity) of its rotational axis (Berger 1978), and the 11-yr sunspot

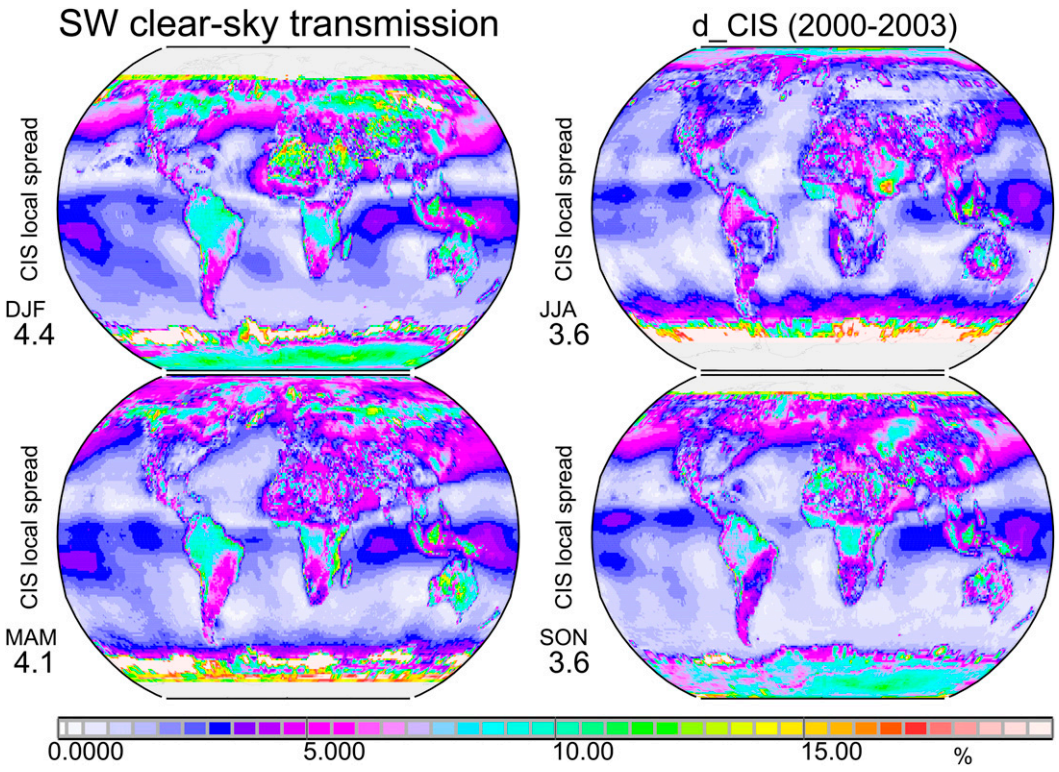

FIG. 2. Seasonal maps of the multiyear (2000–03) local spread among CERES, ISCCP, and SRB datasets (ΔCIS) for the cloud-free atmospheric effective SW transmittance (%). Values below the labels indicate the seasonal global average spread. The noisy pattern over the southern circumpolar belt is caused by data problems in one of the three datasets. The mean clear-sky transmission is on the order of 50%–70%.

cycle. This new TSI value corresponds to 340.2 W m^{-2} for the average annual insolation on a sphere. The CIS average in comparison is slightly larger by about 1.5 W m^{-2} since the CIS average insolation is based on older TSI estimates near 1367 W m^{-2} (Lee et al. 1991; Neckel and D. Labs 1984). The local spread ΔCIS is within 1 W m^{-2}, except over higher latitudes where larger differences are associated with different treatments of averages at very low sun elevations (Raschke et al. 2005).

2) TREATMENT OF AEROSOLS

The effective clear-sky SW atmospheric transmittance is reduced by molecular scattering, by trace gas absorption, and by scattering and absorption of aerosols. Typical SW clear-sky transmission values (annual averages of daily averages) are 60%–75%. Higher values occur over higher surface elevations and aerosol poor locations. Since there should be little disagreement over usually well-understood trace-gas absorption and Rayleigh scattering (but see Oreopoulos et al. 2012), most of the local spread in clear-sky SW transmission is expected to be associated with different representations of aerosol amounts and properties. The globally averaged local spread of SW clear-sky transmission (Fig. 2) in CIS is about 4%. This translates into an average difference in the surface clear-sky SW fluxes of about 12 W m^{-2} (cf. Zhang et al. 2010). The ΔCIS values are smaller over oceans than over continents, especially over regions (and seasons; not shown) where stronger aerosol attenuation is expected. For example, these include regions around the Southern Hemispheric continents (biomass burning), of the Sahara (dust sources), and of the northern Pacific (intercontinental aerosol transport). The larger local spread over higher latitudes during Northern Hemispheric winters is surprising, but is related to a compensating bias in the SW surface albedo in one dataset.

3) SW SURFACE ALBEDO

The effective broadband SW surface albedo (i.e., the ratio of upward and downward fluxes at the surface) is about 13% in the global annual average with strong regional and seasonal modulations. The surface albedo is relatively small (<8%) over oceans but somewhat larger over continents with vegetation, larger still (>30%) over deserts, and largest over snow and ice. The seasonal SW surface albedo local spread (Fig. 3) is about 5%. This translates into an average uncertainty for

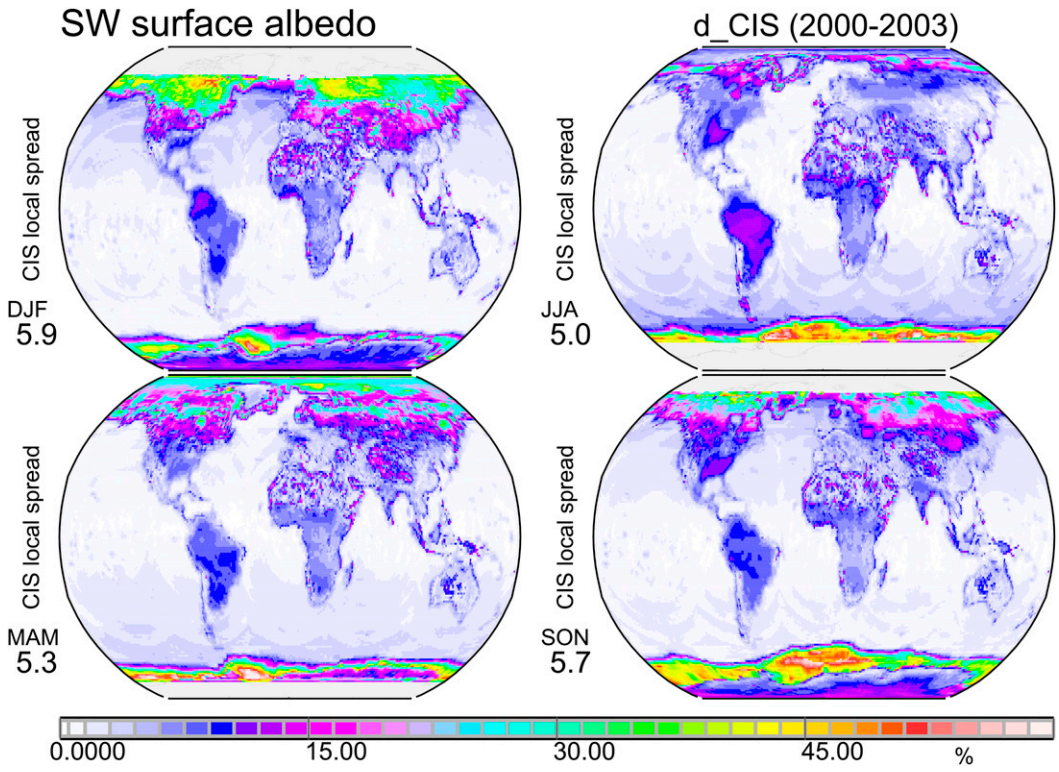

FIG. 3. As in Fig. 2, but for the SW effective surface albedo (%). The mean surface albedo over oceans is 5%–8% and over continents is 15%–40%.

upward SW (hereinafter SW, up) fluxes of about 10 W m^{-2} under all-sky conditions. Almost all larger differences occur over continents; ΔCIS is largest at higher and polar latitudes in winter when snow and ice cover are present. The weak circular anomaly patterns over oceans in Fig. 3 are caused by inconsistencies in the treatment of the view-angle dependence in geostationary data in one dataset.

4) SURFACE TEMPERATURE/LW SURFACE EMITTANCE

The upward LW (hereinafter LW, up) radiative flux from the surface is defined by the surface (skin) temperature and LW emittance and reflectance of the surface. The average upward LW fluxes are near 400 W m^{-2} with maxima in the tropics and much smaller values toward (colder) higher latitudes. The annually averaged CIS spread (Fig. 4) is about 14 W m^{-2}. This corresponds to an average surface temperature spread of about 3 K (Zhang et al. 2006, 2007a). Larger seasonal mean local spreads occur over continents, especially over desert regions (related to spreads for the assumed surface temperature and for the assumed spectral infrared emittance), where the spread frequently exceeds 60 W m^{-2} (or 10 K in surface temperature). Large differences are also detected at higher latitudes during colder seasons.

The ΔCIS of the ancillary datasets is significant, so extra effort is needed to investigate the causes of these differences and to replace poor or inconsistent ancillary input datasets. The resulting differences in calculated surface fluxes reduce the capability of these products to serve as references for modeling.

b. Radiative fluxes at the TOA

Global TOA flux averages for CERES, ISCCP, and SRB, as well as ERBE, are listed in Table 1 for different multiyear periods. The differences in the global averages between different multiyear periods for the same dataset are small compared to the dataset-to-dataset differences for the same time period. Thus, the particular choice of the multiyear period is only of secondary importance.

The approximation of near-zero values for global annual radiative net fluxes at the TOA is fulfilled by all datasets. A slightly larger imbalance for the CERES version used here has been addressed and corrected in the more recent CERES-EBAF version [where EBAF stands for energy balanced and filled; see Loeb et al. (2009)]. Loeb et al. (2009) indicate (their Table 4) that

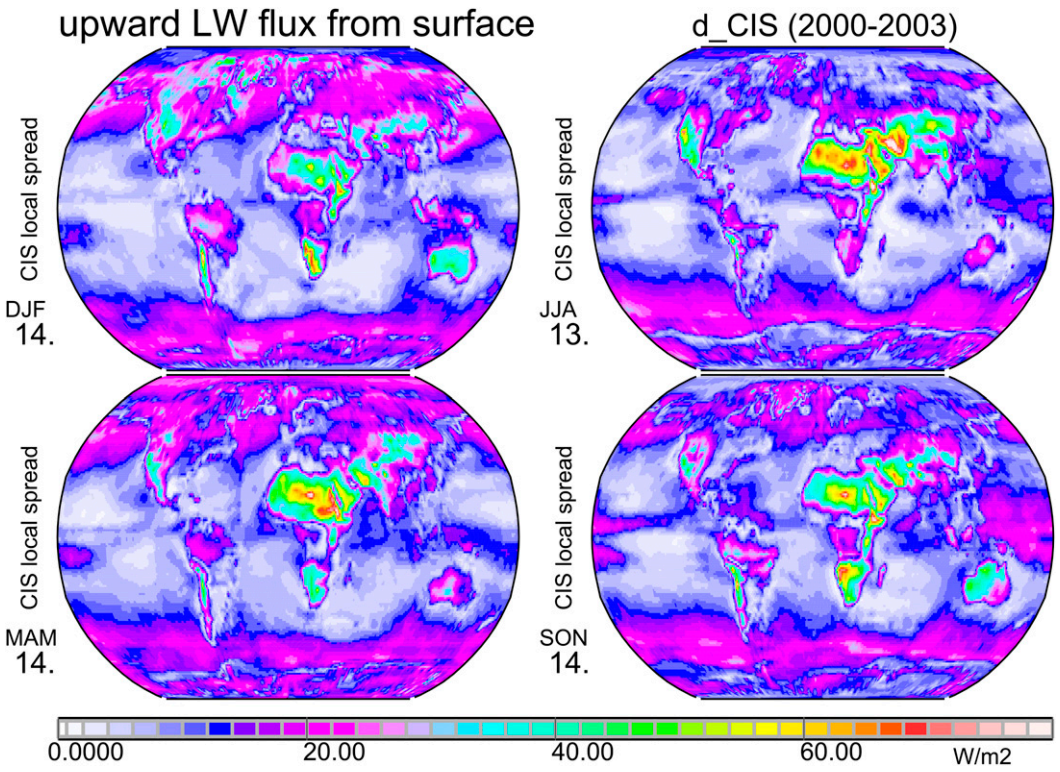

FIG. 4. As in Fig. 2, but for LW effective upward radiative fluxes from the surface.

the adjusted multiyear (March 2000–February 2006) average all-sky TOA SW and LW upward fluxes of CERES are near −100 and near −240 W m^{-2}, respectively.

About 30% of the incoming solar energy is reflected back to space, half of that by clouds. LW thermal energy losses to space are about 2.4 times larger than SW energy losses to space, but the cloud effect on LW thermal energy losses is only about 10%. Comparing SW and LW cloud effects at the TOA, LW energy gains to the Earth–atmosphere system by clouds amount to only about half of the SW (reflection) energy losses attributed to clouds, so that clouds on average cool the planet.

TABLE 1. Comparisons of global multiyear (all sky) radiative flux averages at the TOA. In addition, averages for cloud-free (clear sky) and cloudy regions (CRE) are given. Listed are total (SW plus LW) net flux, SW upward flux, and LW upward flux. ISCCP and SRB data are presented for two different time periods (1984–95 and 2000–03). For the last period the CERES data and the CERES, ISCCP, and SRB average (CIS) are also displayed. CERES and ERBE data from different periods are also compared for data between 60°N and 60°S. By definition, downward fluxes are positive and upward fluxes are negative. The last row lists global averages of the local spread between CERES, ISCCP, and SRB (ΔCIS).

	(SW + LW) net			SW, up			LW, up		
At the TOA (W m^{-2})	All sky	Clear sky	CRE	All sky	Clear sky	CRE	All sky	Clear sky	CRE
ERBE* (1985–88)	21	41	−25	−101	−48	−53	−240	−267	27
CERES* (2000–03)	22	45	−23	−96	−46	−50	−244	−272	28
ISCCP (1984–95)	2.8	27	−24	−106	−56	−50	−233	−259	26
SRB (1984–95)	−0.4	18	−19	−102	−55	−47	−240	−268	28
CERES (2000–03)	6.4	29	−23	−98	−52	−46	−237	−263	27
ISCCP (2000–03)	1.2	26	−25	−105	−54	−51	−235	−262	26
SRB (2000–03)	−1.4	18	−19	−102	−54	−48	−240	−268	27
CIS (2000–03)	2.1	24	−22	−101	−53	−48	−238	−264	27
ΔCIS (2000–03)	12	15	12	11	11	10	7	10	5

* Averages for the region from 60°N to 60°S only.

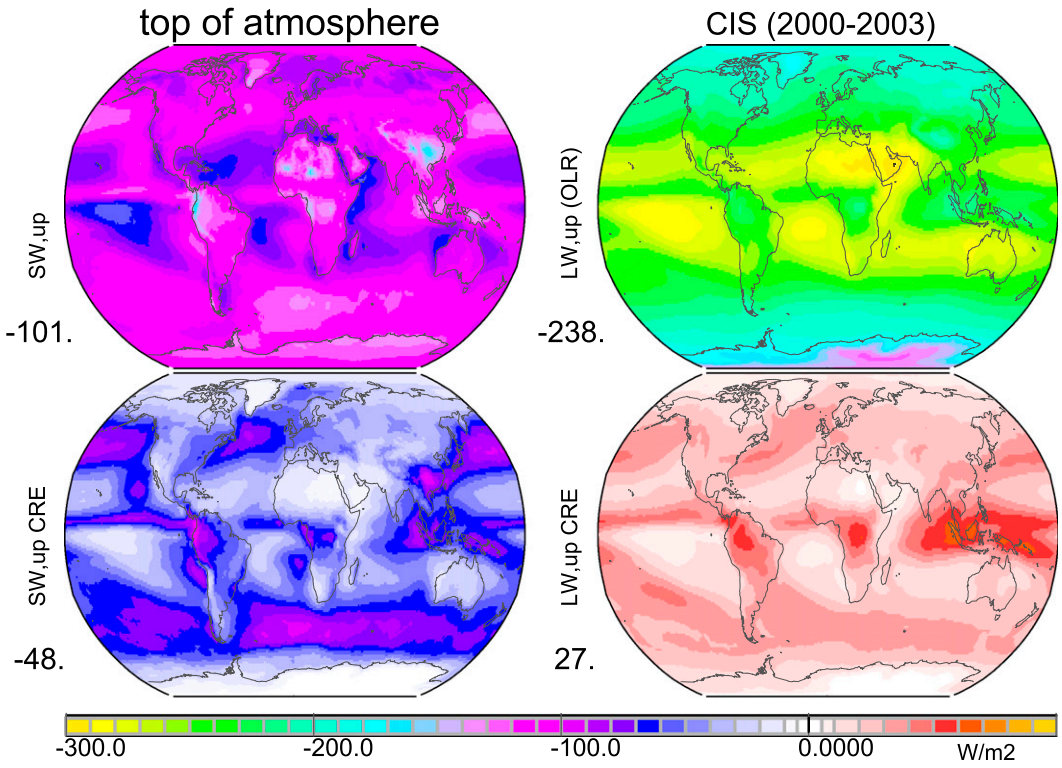

FIG. 5. Multiyear (2000–03) annual CIS radiative flux averages at the TOA for upward (left) shortwave and (right) longwave fluxes for (top) radiative fluxes at all-sky conditions and (bottom) contributing cloud impacts (CRE). Values below the labels indicate global averages. By definition all upward fluxes are negative, so that negative values of upward SW CRE refer to an increase and positive values of upward LW CRE refer to a decrease in clear-sky fluxes.

Figure 5 details the CIS's spatial distribution of annual mean upward SW and LW radiative fluxes at the TOA and the effects of clouds on both. Upward SW fluxes have relatively weak latitudinal but significant longitudinal variability (annual mean). Upward SW fluxes are larger over continents, especially over arid regions. Upward LW fluxes have zonal maxima over the subtropics and minima over polar regions, especially over Antarctica. Zonal modulations are mainly caused by clouds. SW CRE maxima (increased upward flux) occur over midlatitude oceans, while LW CRE maxima (decreased upward flux) occur over areas of tropical convection (with cold cloud tops).

The average local ΔCIS is much larger than differences in the global averages among the datasets. This indicates that the dataset differences are related to regional (and seasonal) features that largely compensate on a global annual scale. The ΔCIS values for both upward SW and (especially) LW fluxes are larger for the clear-sky fluxes than for all-sky fluxes or CREs. Considering that CREs and clear-sky fluxes combine into all-sky fluxes, this means that cloud effects reduce the spread, implying better relative agreement among these datasets for cloud radiative properties than for atmospheric and surface properties.

c. *Radiative fluxes at the surface*

Global multiyear-average surface fluxes for CERES, ISCCP, and SRB, along with the CIS values and the average local ΔCIS, are listed in Table 2. In addition, all-sky flux averages are split into their clear-sky and CRE components. A comparison of the latter two subcomponent averages indicates that clouds on average reduce the downward SW fluxes at the surface by about 25% and increase downward LW (hereinafter LW, dn) fluxes at the surface by about 10%. As with TOA fluxes, the ISCCP and SRB averages for different multiyear periods indicate that time period choices are of secondary importance compared to differences among the datasets.

Net radiative fluxes at the surface indicate large imbalances of about $115\,\mathrm{W\,m^{-2}}$ globally when annually averaged. This imbalance is offset primarily by latent heat release and, secondarily, by the release of sensible heat and also by a small ocean heat uptake. The differences in the surface net radiative fluxes among the three observational datasets are larger than those for TOA fluxes. In particular, the differences among the CRE and

TABLE 2. Comparisons of global multiyear (all sky) radiative flux averages at the surface. In addition, averages for cloud-free (clear sky) and cloudy regions (CRE) only are given. Listed are total (SW plus LW) net flux, SW downward flux, SW upward flux, LW downward flux, and LW upward flux. ISCCP and SRB data are presented for two different time periods (1984–95 and 2000–03). For the last period the CERES data and the CERES, ISCCP, and SRB average (CIS) are also displayed. By definition, downward fluxes are positive and upward fluxes are negative. The last row lists global averages of the local spread between CERES, ISCCP, and SRB (ΔCIS).

	(SW + LW) net			SW, dn			SW, up			LW, dn			LW, up		
At the surface ($W m^{-2}$)	All sky	Clear sky	CRE	All sky	Clear sky	CRE	All sky	Clear sky	CRE	All sky	Clear sky	CRE	All sky	Clear sky	CRE
ISCCP (1984–95)	115	139	−23	189	247	−58	—	—	—	343	312	31	−393	−392	−1.5
SRB (1984–95)	113	127	−15	186	242	−56	—	—	—	343	307	36	−396	−395	−0.5
CERES (2000–03)	123	136	−13	195	244	−50	−24	−30	6	344	313	31	−392	−391	0
ISCCP (2000–03)	118	142	−24	189	248	−59	−23	−30	7	345	314	31	−393	−391	−1
SRB (2000–03)	112	129	−17	186	243	−57	−21	−27	6	343	308	35	−397	−396	0
CIS (2000–03)	117	135	−18	190	245	−55	−23	−29	6	344	312	32	−394	−393	0
ΔCIS (2000–03)	23	25	17	16	12	15	3	–	2	13	4	8	14	14	2

clear-sky subcomponents are at least as large as the differences for the all-sky fluxes. Despite the larger differences in the surface radiative imbalances among the observational datasets, they are all larger than in climate modeling (see section 3), which raises concerns that climate modeling might underestimate latent heat release and precipitation.

The spatial distributions of CIS for downward SW and LW fluxes at the surface and contributions by clouds (CREs) are detailed in Fig. 6. Downward SW and LW flux annual averages are largest in the tropics and decrease toward the poles. SW zonal anomalies are caused mainly by cloud variations. SW CRE maxima (flux decreases) occur over midlatitude oceans, areas of tropical convection, and central China. LW CRE maxima (flux increases) occur mainly over midlatitude and subpolar oceans. The variation of clouds produces only relatively small LW zonal anomalies in comparison with the effects of surface temperature variations (e.g., continent versus ocean). The global average local ΔCIS for downward radiative fluxes at the surface in Table 2 is larger than that for upward fluxes at the TOA in Table 1. This was expected, as more ancillary data are required for the determination of surface radiative fluxes (with more potential problems). The subcomponent spread indicates that the representation of clouds is the main contributor to ΔCIS for downward SW fluxes, while the clear-sky spread (mainly over deserts, as illustrated in Fig. 4) suggests that surface temperature is the main contributor to ΔCIS for upward LW fluxes.

The utility of the three observational datasets (and CIS) as references for radiative fluxes at the surface is reduced by inconsistencies in applied ancillary datasets. Thus, CIS downward radiative fluxes at the surface are further evaluated using the calibrated surface radiation monitoring by the Baseline Surface Radiometer Network (BSRN; Dutton et al. 2001; Ohmura et al. 1998; Roesch et al. 2011). Monthly BSRN statistics from samples between 1996 and 2002 (Wild et al. 2009) are used as a reference. Any agreement to within $10 W m^{-2}$ is deemed acceptable, considering the unresolved issues with the area representativeness of the BSRN sites (Hakuba et al. 2013).

Figure 7 displays annual differences in CIS with ground measurement statistics at 28 BSRN sites for the downward flux properties in Fig. 6. Most stations are over Europe and the United States. There and also over Japan and Australia (thus likely over urban continental midlatitudes at least for the Northern Hemisphere), the CIS atmosphere is slightly less transparent as downward SW fluxes are on the low side. Interestingly, the downward SW CRE (note its negative sign) is much smaller for CIS in that region. As a result, the CIS clear-sky attenuation has to be much larger, which indicates to us a too strong aerosol loading (by pollution) over the northern midlatitudes. The derived aerosol tendencies (SW fluxes more transparent than CRE underestimates) are quite the opposite for tropical regions as well as for regions of South Africa and South America, where aerosol loading (by biomass burning) is too weak. For downward LW fluxes most CIS data at BSRN sites are in good agreement with the observational statistics, with a tendency toward underestimates over the United States and Europe. The single major exception occurs over the Sahara Desert. There (also in the absence of clouds and water vapor) the stronger downward LW fluxes reflect CIS overestimates to surface temperature and surface emittance over deserts. Aerosols as a potential cause can be excluded since two of the three datasets contributing to CIS ignore aerosol longwave effects.

Figure 8 displays for downward SW fluxes the seasonal differences in CIS minus BSRN. Seasonal differences are more diverse than annual differences. Larger differences are especially observed during winter (e.g.,

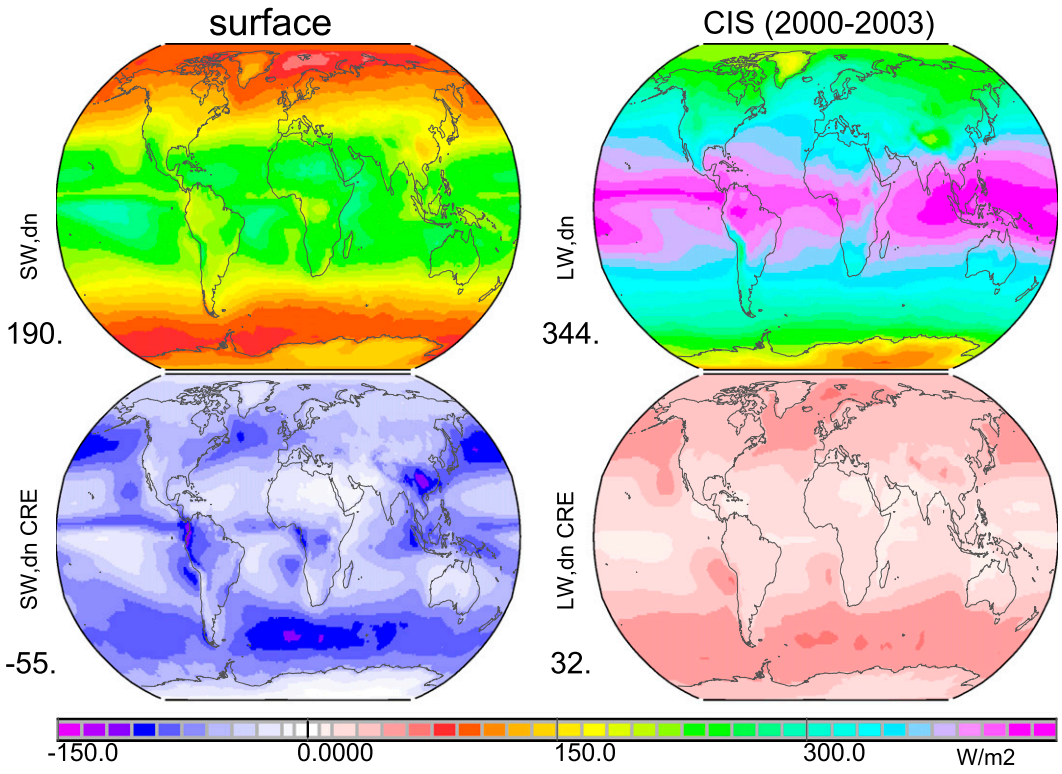

FIG. 6. As in Fig. 5, but at the surface for downward shortwave and downward longwave. By definition all downward fluxes are positive, so that negative values of downward shortwave CRE refer to a decrease and positive values of downward longwave CRE refer to an increase in clear-sky LW, dn.

East Asia) or summer (e.g., eastern United States). Some of these differences are unacceptably large, but it remains unclear to what degree sampling differences or representativeness artifacts have introduced biases.

The comparisons against ground-based data are handicapped by uncertainties in the area representativeness of point measurements, the uneven site distribution over the globe, and the small number of network surface reference sites. Thus, stronger reference capabilities require 1) more high-quality (BSRN type) ground network (radiation) sites; 2) better global coverage, especially over oceans; 3) more evaluations of the area representativeness of the individual site statistics; and 4) better parameterizations of the radiative properties of structured land surfaces.

d. Net fluxes

The global average CIS and ΔCIS TOA and surface net fluxes are summarized in Fig. 9, together with their spatial distributions at the TOA (top panel) and surface (bottom panel).

The CIS TOA net flux spatial pattern shows surpluses and deficits over the entire globe. The meridional gradient, mainly caused by the distribution of available solar energy at the TOA, is modulated by clouds and the continental heat islands. Low clouds (e.g., central China) or warm cloud-free deserts (e.g., Sahara) tend to exhibit net flux losses, while high-altitude cloud regions (central tropics) tend to exhibit net flux surpluses. Similar patterns from satellite remote sensing were obtained as early as 40 years ago in an analysis of *Nimbus-3* satellite data (Raschke et al. 1973). The tropical and subtropical TOA net flux surplus in combination with higher-latitude deficits forces an atmosphere–ocean circulation that produces a mean meridional energy transport that is largest near latitudes of 35°N and 35°S (Zhang and Rossow 1997; Zhang et al. 2007b).

The CIS surface net flux spatial pattern displays positive values varying between zero and more than 200 $W m^{-2}$. The largest values occur over tropical oceans, relatively low values occur over drier subtropical regions (e.g., deserts), and the smallest values occur over the polar regions.

e. Atmospheric budgets

Figure 9 also displays the global CIS net radiative flux averages in the atmosphere calculated from the differences between TOA and surface fluxes in terms of two

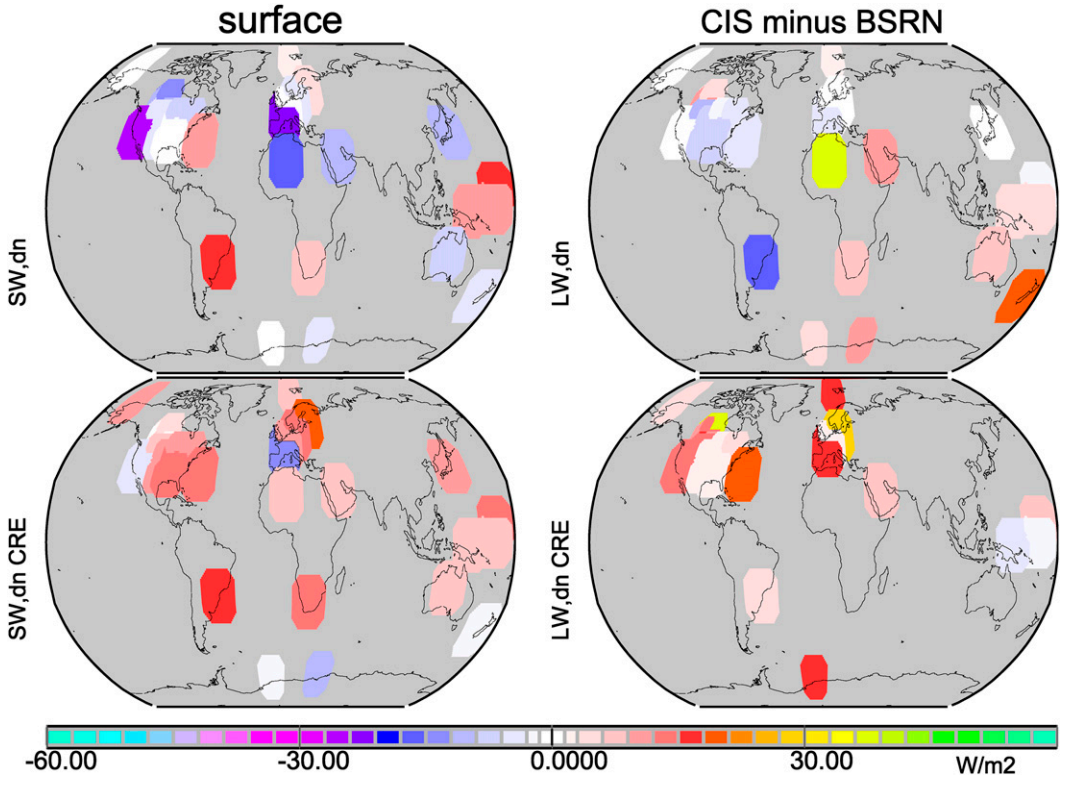

FIG. 7. Multiyear (2000–03) annual differences in CIS downward fluxes (from Fig. 6) to local ground data statistics at 28 BSRN surface sites. Note that downward shortwave CREs are negative by definition so that a positive bias indicates an underestimate.

quantities: the atmospheric net flux divergence (DIV) and the greenhouse effect (GH), defined by the difference in the upward LW fluxes at the TOA and surface. For these properties multiyear flux averages for CERES, ISCCP, SRB, their average, CIS, and the average ΔCIS are listed in Table 3, together with the SW (heating) and LW (cooling) components.

The divergence is negative (globally averaged about $-115\,\mathrm{W\,m^{-2}}$), indicating an overall radiative cooling of the atmosphere: the positive SW atmospheric heating of about $+75\,\mathrm{W\,m^{-2}}$ (corresponding to 22% of the incoming downward SW flux at TOA) is more than offset by a larger negative LW cooling of about $-190\,\mathrm{W\,m^{-2}}$. Cloud effects on DIV are small. The influence of clouds on the SW absorption is small because the reduction of atmospheric absorption by water vapor below clouds is largely offset by the additional absorption within and above clouds. Cloud effects on the global average LW atmospheric cooling are also small because LW cooling by lower-altitude (stratocumulus) clouds and clouds at higher latitudes are compensated by LW warming by higher clouds at lower latitudes, especially over the eastern tropical Pacific.

The GH retains about 40% of the LW surface upward fluxes released at the surface in the Earth–atmosphere system. Cloud contributions to the GH are on average only about 18%. Most of the GH contributions are from trace gases such as water vapor, carbon dioxide, and ozone.

Figure 10 details the spatial distributions of the CIS DIV and GH, as well as contributions by clouds (CRE) to both quantities. The DIV maxima occur over stratocumulus decks off of continental west coasts in the subtropics and DIV minima occur over arid continental regions, the tropical western Pacific, and Antarctica. The CRE of DIV, when globally averaged, is very small. However, negative LW contributions at higher latitudes and over stratocumulus decks are largely offset by positive LW contributions over the tropics and especially over the western Pacific.

The GH exhibits a strong latitudinal gradient. The largest contributions are over tropical regions where there is strong convection, most prominently over the western Pacific. Relatively small contributions occur over the polar regions, especially over Antarctica. The GH spatial patterns are strongly influenced by clouds, which is very similar (not surprisingly) to the cloud impacts on upward LW fluxes at the TOA (cf. with Fig. 2). Global averages of the local spread for DIV and GH, shown in Table 3, are as large as those for downward surface fluxes in Table 2. But unlike for the downward

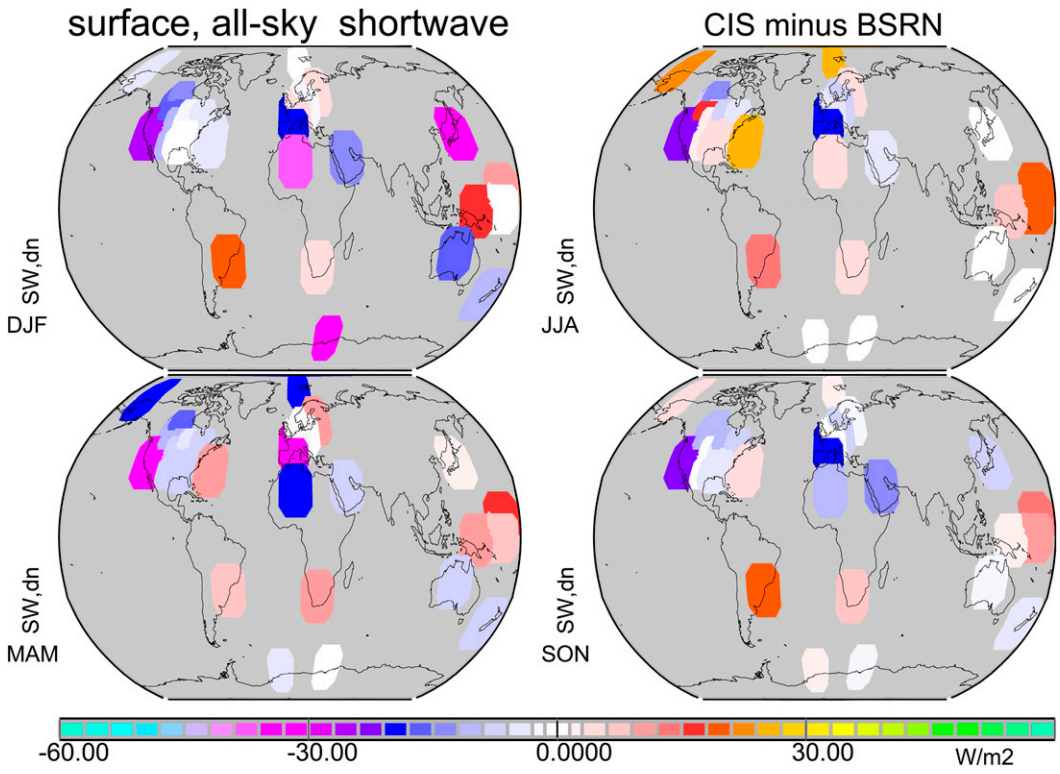

FIG. 8. Multiyear (2000–03) seasonal differences for measured all-sky downward shortwave radiative fluxes at the surface between CIS and ground data statistics at 28 BSRN surface sites.

fluxes (where larger local spread contributions are related to clouds), now the larger spread contributions are associated with cloud-free conditions and thus ancillary data. The main contributors to the DIV spread are the absorption of solar radiation by aerosols for the SW DIV and the surface properties of temperature and emittance for the LW DIV. The use of more accurate and more consistent ancillary data, which is also consistent with other applied ancillary data, certainly raise the scientific value and reference status for the modeling of observational datasets.

f. Ocean versus land fluxes

To better understand the radiative energy distributions in the Earth–atmosphere system, the CIS dataset has been subdivided into two subsets according to the underlying surface. The ''ocean'' dataset combines deep ocean (surface albedo $< 8\%$) areas with no ice cover during the year (57.6% coverage), while the remaining surface area (42.4% coverage) is called the ''land'' dataset. For selected radiative flux components, the CIS regional subset averages for ocean and land are compared in Table 4 within the context of the CIS global averages. The incoming solar radiation for ocean areas is $364.2\,\mathrm{W\,m^{-2}}$ and for land areas it is $310.9\,\mathrm{W\,m^{-2}}$. Thus, to better compare radiative energy flows over oceans and land, all flux properties (including their clear-sky and CRE) are scaled by the average incoming radiation at the TOA. Larger scaled flux differences between land and ocean in Table 4 are specially marked.

The major differences between land and ocean are the larger SW surface albedo (about 24% over land versus about 5% over ocean) and the higher elevation of the continents, resulting in a geometrically thinner atmosphere. The albedo difference explains the larger upward SW fluxes and smaller net SW fluxes at the surface and TOA (planetary albedo of about 35% over land versus about 26% over ocean). The elevated topography over continents with less atmospheric column water vapor is the major reason for stronger upward LW fluxes at the TOA and weaker GH over continents. Other significant differences are the generally warmer surface temperatures over continents and the larger (mainly low altitude) cloud cover over oceans (Stubenrauch et al. 2013). These differences explain the relatively larger upward LW fluxes at the surface over continents and the relatively weaker cloud contributions to the upward SW flux at the TOA over continents.

Net fluxes at TOA indicate warming over oceans and cooling over land. Both SW and LW effects contribute

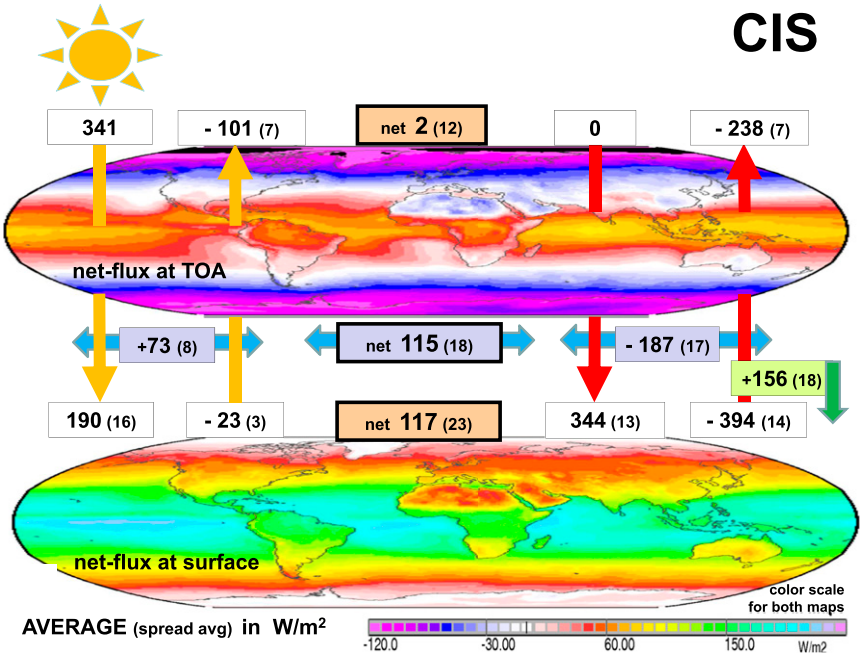

FIG. 9. Global multiyear (2000–03) annual averages of CIS (and ΔCIS, in parentheses) all-sky SW (white boxes on left side of figure) and LW (white boxes on right side of figure) net radiative fluxes. By definition all downward fluxes are positive and upward fluxes are negative. Also indicated are averages for net budgets at the surface and TOA (beige boxes), atmospheric budgets (divergence; lavender boxes), and the greenhouse effect (green box). The two maps display annual CIS net budget distributions at the TOA and at Earth's surface.

to this difference. Continental cooling, despite less cloud cover, is caused by a larger surface albedo and a reduced clear-sky GH (less water vapor). Oceanic warming, despite more cloud cover, is caused by a smaller surface albedo and a stronger clear-sky GH (more water vapor).

The net flux imbalances at the surface are larger over oceans than over land. Both SW and LW effects contribute to this difference, too. The main reasons are smaller upward fluxes over oceans, which are mainly due to a smaller SW surface albedo and to relatively lower surface temperatures over oceans.

3. Climate modeling differences with CIS

Global climate models simulate the hydrological cycle and radiative energy exchanges, so broadband radiative fluxes at the TOA and at the surface are available as output. The models are constrained to balance the global annual mean net radiation at the TOA. Thus, while the TOA averages are expected to closely agree with CIS, averages for the surface and atmosphere, as well as their spatial distributions, may not. This section investigates the differences found when global modeling with CIS.

The characteristic radiative flux averages and their spatial distributions from modeling used in this study are based on the ensemble output from the CMIP3 modeling exercise (Gates et al. 1999), conducted in conjunction with the IPCC's Fourth Assessment Report. For each month, the 25th and 75th percentile values in the 20-member ensemble distributions are averaged and differenced at each map grid point (1° × 1°) over the period 1980–99. For all relevant radiative flux components, the averages are referred to as the CMIP3 global fields, and the differences (ΔCMIP3) are used to estimate modeling uncertainty. These quantities are relatively more stable as the extreme (local) behaviors of individual models are removed. Using the older CMIP3 model output, despite newer exercises such as CMIP5, is still meaningful, since the general behavior with respect to radiative flux averages and their spatial patterns has not changed significantly (Li et al. 2013; Wild 2008; Wild et al. 2012). In the following comparisons, it is assumed that CIS is more likely to be a good reference at TOA but may be less reliable at the surface where extra modeling and ancillary data must be used.

a. Ancillary data

For the radiative fluxes at the surface and in the atmosphere only the larger differences between CMIP3 and CIS may be meaningful, as both have limitations as a result of the use of ancillary data.

TABLE 3. Comparisons of global multiyear (all sky) radiative flux averages for the atmosphere. In addition, averages for cloud-free (clear sky) and cloudy regions (CRE) only are given. Listed are averages for the total (SW plus LW) net divergence, its SW (warming) and LW (cooling) contributions, and the greenhouse effect. ISCCP and SRB data are presented for two different time periods (1984–95 and 2000–03). For the last period CERES data and the CERES, ISCCP, and SRB average (CIS) are also displayed. By definition, downward fluxes are positive and upward fluxes are negative. The last row lists global averages of the local spread between CERES, ISCCP, and SRB (ΔCIS).

	(SW+LW) DIV			SW DIV			LW DIV			GH		
In the atmosphere ($W\,m^{-2}$)	All sky	Clear sky	CRE	All sky	Clear sky	CRE	All sky	Clear sky	CRE	All sky	Clear sky	CRE
ISCCP (1984–95)	−113	−112	−1	71	68	3	−183	−179	−4	160	133	27
SRB (1984–95)	−113	−109	−4	75	72	3	−188	−181	−7	156	127	29
CERES (2000–03)	−116	−107	−9	73	77	−4	−189	−185	−4	155	129	26
ISCCP (2000–03)	−117	−116	−1	71	68	3	−187	−183	−4	158	130	28
SRB (2000–03)	−112	−108	−4	74	71	3	−186	−180	−6	156	128	28
CIS (2000–03)	−115	−111	−5	73	72	1	−187	−183	−5	156	129	27
ΔCIS (2000–03)	18	23	15	8	15	12	17	19	10	18	17	7

The effective clear-sky SW atmospheric transmission in CMIP3 data is significantly larger than in CIS. Globally, the differences amount to $9\,W\,m^{-2}$ or 3%. Larger differences occur over continents and point to the treatment of aerosols. This conclusion is also supported by the analysis in Fig. 7 and calls for more appropriate aerosol ancillary data.

The effective SW surface albedo in CMIP3 is larger than in CIS, which could partially offset the larger SW atmospheric transmission in modeling except that these differences are not always collocated. There is good agreement over oceans, but over continents there are larger disagreements of both signs. CMIP3 tends to display smaller effective surface albedos over deserts but larger values at high latitudes, especially during the winter and spring over NH continents when snow is present. Figure 3 illustrated a range ΔCIS of than 40% during boreal winters. Such large diversity

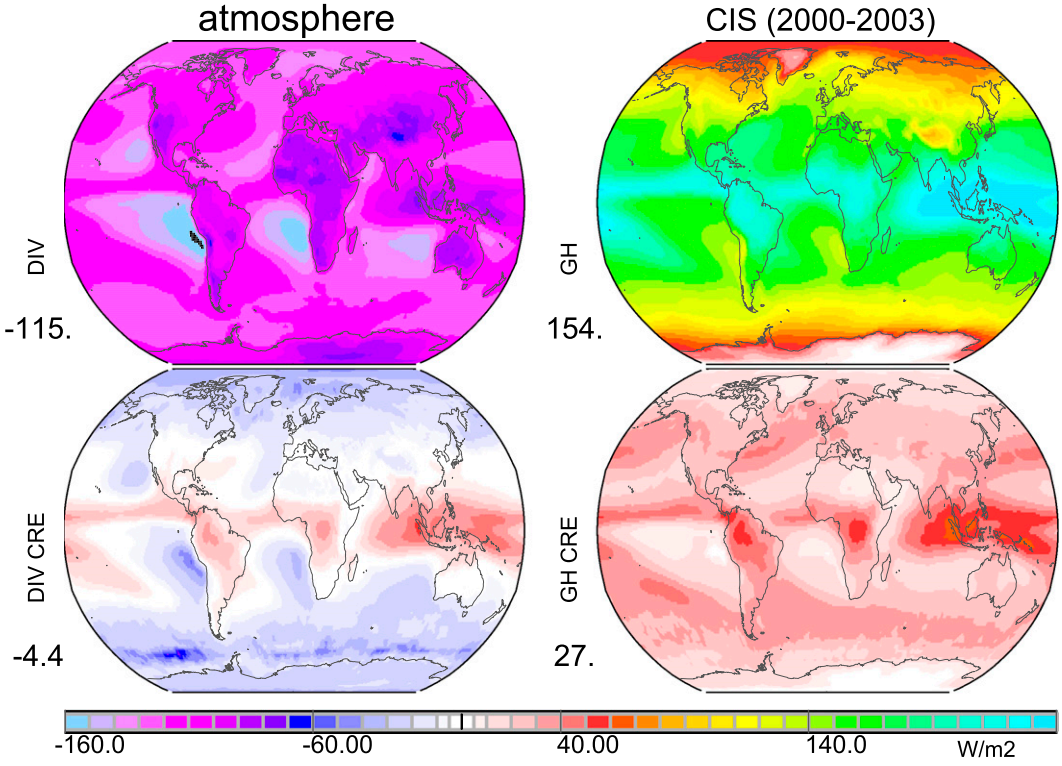

FIG. 10. Multiyear (2000–03) values of annual CIS (left) atmospheric net DIV and (right) LW GH (top) during all-sky conditions and (bottom) for the contributing CRE. Values below the labels indicate global averages.

TABLE 4. Multiyear radiative flux products scaled to average shortwave downward (SW, dn) fluxes at the TOA for all-sky conditions and for all-sky subcomponents of cloud-free regions (clear sky) and cloudy regions (CRE). For CIS (the average from CERES, ISCCP, and SRB satellite data), the global averages (boldface roman font) are compared with CIS averages only over oceans and land, where italics highlight CIS land data differences (from ocean data) that deviate by more than 3% (or 0.03). The CIS ocean and land averages are also compared with ocean and land averages of CMIP3 (central values from CMIP3 global modeling), where boldface italics indicate differences (from CIS) of more than 3% (or 0.03). Rounding errors are ±0.01. By definition, downward fluxes are positive and upward fluxes are negative. Here, S is the mean annual insolation at the TOA over the globe and over its continental and ocean fractions.

Selected radiative flux products scaled to SW, dn at the TOA	All sky					Clear sky					CRE				
	CIS	CIS		CMIP3		CIS	CIS		CMIP3		CIS	CIS		CMIP3	
	global (S = 342)	Ocean (S = 364.2)	Land (S = 310.9)	Ocean (S = 342)	Land (S = 310.9)	global (S = 342)	Ocean (S = 364)	Land (S = 310.9)	Ocean (S = 364.2)	Land (S = 310.9)	global (S = 342)	Ocean (S = 364.2)	Land (S = 310.9)	Ocean (S = 364.2)	Land (S = 310.9)
Total, net at TOA	**0.01**	0.06	*−0.08*	0.06	−0.07	**0.07**	0.14	*−0.03*	0.13	−0.04	**−0.07**	−0.08	*−0.05*	−0.08	−0.04
SW, up at TOA	**− 0.30**	−0.26	*−0.35*	−0.28	−0.35	**−0.15**	−0.11	*−0.22*	−0.11	−0.23	**−0.14**	−0.15	*−0.12*	−0.17	−0.12
LW, up at TOA	**−0.70**	−0.68	*−0.73*	−0.67	−0.72	**−0.77**	−0.75	*−0.81*	−0.75	−0.80	**0.07**	0.07	0.08	0.08	0.08
SW, dn at surface	**0.56**	0.56	0.55	0.54	0.56	**0.72**	0.73	0.71	0.74	***0.74***	**−0.16**	−0.17	−0.16	***−0.21***	−0.18
SW, up at surface	**−0.07**	−0.02	*−0.13*	−0.04	−0.14	**−0.09**	−0.05	*−0.15*	−0.06	−0.17	**0.02**	0.02	0.02	0.02	0.03
LW, dn at surface	**1.01**	1.01	1.00	0.99	***0.95***	**0.91**	0.92	0.90	0.91	***0.86***	**0.09**	0.09	0.10	0.08	0.09
LW, up at surface	**−1.15**	−1.14	*−1.17*	−1.15	−1.15	**−1.15**	−1.14	−1.17	−1.15	−1.15	**0.00**	0.00	0.00	0.00	0.00
SW, net at surface	**0.49**	0.54	*0.42*	***0.50***	0.42	**−0.61**	0.68	*0.56*	0.68	0.57	**−0.14**	−0.15	−0.14	***−0.19***	−0.15
LW, net at surface	**−0.14**	−0.13	*−0.17*	***−0.16***	***−0.20***	**−0.24**	−0.22	*−0.27*	−0.24	−0.29	**0.09**	0.09	0.10	0.08	0.09
Total, net at surface	**0.34**	0.40	*0.26*	***0.35***	***0.23***	**0.40**	0.46	*0.29*	0.46	0.28	**−0.05**	−0.07	*−0.03*	***−0.11***	−0.05
SW, DIV in atmosphere	**0.21**	0.21	0.22	0.22	0.22	**0.21**	0.21	0.22	0.20	0.20	**0.00**	0.00	0.02	0.02	0.02
LW, DIV in atmosphere	**−0.55**	−0.54	−0.56	−0.52	***−0.53***	**−0.53**	−0.53	−0.54	−0.52	−0.52	**−0.01**	−0.01	−0.02	0.01	−0.01
Total DIV in atmosphere	**−0.34**	−0.34	−0.34	***−0.29***	***−0.30***	**−0.32**	−0.33	−0.32	−0.32	−0.31	**−0.01**	−0.01	−0.01	***0.03***	0.01
GH at TOA	**0.45**	0.46	*0.43*	0.48	0.43	**0.37**	0.38	*0.35*	0.40	0.35	**0.08**	0.08	0.08	0.08	0.08

TABLE 5. Comparisons of multiyear averages and averages of local spread (italics) for radiative flux products at the TOA between typical values from satellite remote sensing (CIS and ΔCIS) and typical values from global modeling (CMIP3 and ΔCMIP3).

	(SW + LW) net			SW, up			LW, up		
At the TOA ($W m^{-2}$)	All sky	Clear sky	CRE	All sky	Clear sky	CRE	All sky	Clear sky	CRE
CIS (2000–03)	2.5	25	−22	−101	−53	−48	−238	−264	27
CMIP3 (1984–95)	0.3	23	−23	−105	−54	−51	−236	−263	27
CMIP3 − CIS	−0.2	−2	1	−4	−1	−3	2	1	0
ΔCIS (2000–03)	*12*	*15*	*12*	*11*	*11*	*10*	*7*	*10*	*5*
ΔCMIP3 (1984–95)	*14*	*9*	*15*	*19*	*9*	*17*	*14*	*7*	*10*
ΔCMIP3 − ΔCIS	*2*	*−6*	*3*	*8*	*−2*	*7*	*7*	*−3*	*5*

will draw the average below expected values. Thus, for the CIS data, the assumed land albedos for snow-covered regions are likely underestimates.

The effective upward LW fluxes (determined by surface temperature and surface emittance) in CMIP3 data are similar in their patterns but lower than CIS over desert regions. For those regions Fig. 4 illustrated a range ΔCIS on the order of 60 $W m^{-2}$. This corresponds to the surface temperature differences of more than 10 K. Unless these large CIS differences are better understood, meaningful comparisons over desert regions are not possible.

b. *Radiative fluxes at the TOA*

Global averages and the spreads of CMIP3 and CIS and their differences for various radiative flux components at TOA are compared in Table 5. Differences are presented for net fluxes and their four components: SW downward, SW upward, LW downward, and LW upward fluxes. In addition, clear-sky fluxes and the CREs are indicated.

The total global mean differences are remarkably small. This reflects the requirement for a balanced TOA energy budget in climate modeling; note, however, that such a constraint was not applied to the CIS products. The average local spreads of TOA net fluxes for climate modeling, ΔCMIP3, and ΔCIS are similar in magnitude. However, the contributions to uncertainty are quite different. In climate modeling, the SW and LW TOA CREs are much more uncertain (larger spread), indicating problems with cloud properties and their spatial distributions. In CIS the clear-sky fluxes are more uncertain, indicating larger diversity among the ancillary data.

Figure 11 details the spatial distributions of the differences between CMIP3 and CIS for the upward SW and LW fluxes at the TOA and the contribution by clouds to both fluxes. There are significant regional differences of both signs, despite the relatively good agreement for global averages. Local SW differences exceed 30 $W m^{-2}$ in many regions. The similarity of the patterns of differences in the CREs and all-sky fluxes indicates that most TOA flux differences are caused by differences in the representation of clouds. The largest CRE differences appear over tropical oceans. In climate modeling, the CREs are smaller over stratocumulus decks, yet larger in the trade wind cumulus regions. These tendencies reveal regional biases in the modeling of cloud properties, since the cloud distributions and CRE patterns are quite consistent in the observational datasets. Another major difference is smaller upward SW fluxes in climate modeling over northern Africa unrelated to clouds, possibly because of assumed weaker aerosol impacts.

c. *Radiative fluxes at the surface*

Global averages and the spreads of CMIP3 and CIS and their differences for radiative fluxes at the surface are compared in Table 6. Differences are presented for net fluxes and their four components: SW downward, SW upward, LW downward, and LW upward fluxes. In addition, clear-sky fluxes and CREs are indicated.

The total global mean net flux imbalance at the surface is 14 $W m^{-2}$ smaller in CMIP3 than in CIS. Both smaller downward SW (−3 $W m^{-2}$) and downward LW (−10 $W m^{-2}$) flux components contribute during the climate modeling process. The downward LW flux differences have similarly strong contributions from cloud-free (−6 $W m^{-2}$) and cloudy conditions (−4 $W m^{-2}$). The downward SW flux differences are composed of larger differences of opposite sign. Much smaller values under cloudy conditions in CMIP3 (−12 $W m^{-2}$) are largely compensated by more transparent (larger) clear-sky fluxes (+9 $W m^{-2}$). These global SW flux tendencies indicate optically thicker clouds and less aerosol in CMIP3 than in CIS. Given larger cloud optical depths in global modeling, the reduced LW radiation back to the surface is surprising, as if cloud-base altitudes in modeling are higher than estimated in CIS. This difference is

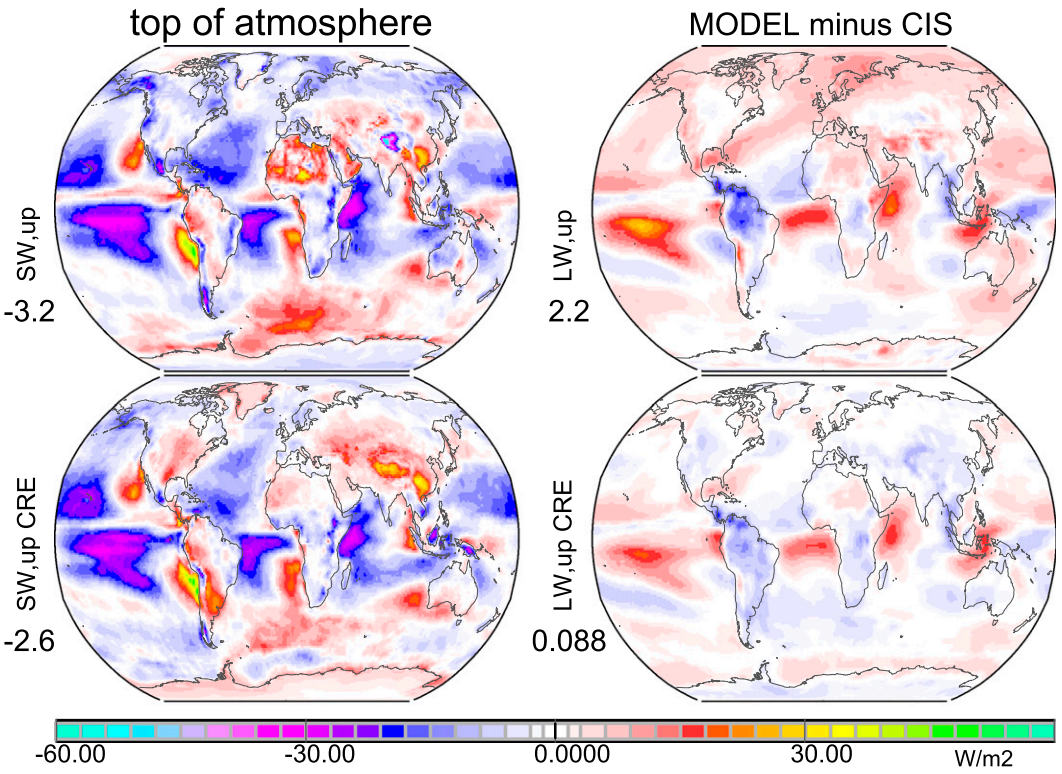

FIG. 11. Differences between annual interquartile averages from CMIP3 global modeling and averages of CIS radiative flux distributions at the TOA for upward (left) SW and (right) LW radiative fluxes during (top) all-sky conditions and (bottom) contributing CRE (cf. with Fig. 5 and Table 5). Note that upward fluxes are by definition negative (e.g., a negative upward flux difference indicates a stronger upward flux in CMIP3 modeling and vice versa). Values below the labels indicate globally averaged differences.

enhanced because the satellite surface flux products have to estimate cloud-base altitudes from external sources and might be expected to overestimate them (cf. Zhang et al. 2004). The local average spread is larger for SW flux components than for LW flux components in both climate modeling and the observational dataset. In climate modeling there is significant diversity in cloud simulations, as ΔCMIP3 values for SW and LW CREs are about twice as large as for ΔCIS, but interestingly not for net flux CREs. The larger ΔCIS under clear-sky conditions is mainly caused by the diversity of the ancillary data used for the surface boundary conditions.

Figure 12 details the spatial distribution of differences between CMIP3 and CIS for downward SW and LW fluxes at the surface and contributions by clouds to these differences. Over oceans, differences in cloud representations (smaller optical depths for stratocumulus and larger optical depths for trade wind cumuli in climate modeling) largely determine the spatial patterns of the differences. Over continents, differences under clear-sky conditions dominate. These are mainly associated with CIS ancillary data deficiencies: larger downward SW fluxes over continents in CMIP3 are likely caused by too-strong CIS aerosol effects (relative to those in CMIP3), and much smaller downward LW fluxes over deserts in CMIP3 are mainly caused by overestimates in temperature and/or emittance in the CIS data (note the large spread in Fig. 4).

Figure 13 compares local uncertainties between climate modeling ΔCMIP3 and observational data, ΔCIS, by showing the ratio [(ΔCMIP3 − ΔCIS)/ΔCIS] for downward SW and LW fluxes and their associated CREs. Note that this approach compares the modeling range as represented by the differences between the 25th and 75th percentiles of the 20 CMIP model ensemble in relation to the full range of observational differences. Positive values indicate that local uncertainty is larger in climate modeling and negative values that uncertainty is larger in the observational data. The uncertainty in global modeling for all surface fluxes is large. The reasons that a stronger global modeling diversity only appears over oceans (e.g., for downward SW fluxes at lower latitudes and for downward LW CREs) is more a reflection of the large uncertainty in the applied ancillary (to aerosol and surface

TABLE 6. Comparisons of multiyear averages and averages of local spread (italics) for radiative flux products at the surface between typical values from satellite remote sensing (CIS and ΔCIS) and typical values from global modeling (CMIP3 and ΔCMIP3).

At the surface ($W m^{-2}$)	(SW + LW) net			SW, dn			SW, up			LW, dn			LW, up		
	All sky	Clear sky	CRE	All sky	Clear sky	CRE	All sky	Clear sky	CRE	All sky	Clear sky	CRE	All sky	Clear sky	CRE
CIS (2000–03)	117	135	−18	190	245	−55	−23	−29	+6	344	312	32	−394	−393	−0
CMIP3 (1984–95)	103	133	−30	187	254	−67	−25	−28	+3	334	306	28	−393	−392	−0
CMIP3 − CIS	−14	−2	12	−3	9	−12	−2	1	−3	−10	−6	−4	1	1	0
ΔCIS (2000–03)	*23*	*25*	*17*	*16*	*12*	*15*	*3*	—	*2*	*13*	*4*	*8*	*14*	*14*	*2*
ΔCMIP3 (1984–95)	*21*	*13*	*13*	*28*	*10*	*23*	*4*	—	—	*19*	*7*	*17*	*13*	—	—
ΔCMIP3 − ΔCIS	*−2*	*−12*	*−4*	*12*	*−2*	*8*	*1*	—	—	*6*	*3*	*9*	*−1*	—	—

properties) in CIS, which has stronger impacts over continents than oceans.

d. *Radiative net fluxes*

Differences between CMIP3 and CIS for global averages for radiative fluxes and their spreads (in parentheses) are summarized in Fig. 14. The corresponding mean net fluxes of CIS are shown in Fig. 9. Complementing these global averages are differences in the spatial distributions of the annual mean net radiative fluxes at TOA (Fig. 14, top) and the surface (Fig. 14, bottom).

The TOA net flux difference spatial patterns in Fig. 14 show compensating surpluses and deficits. Positive values indicate regions where the upward radiative fluxes at the TOA are smaller in CMIP3 than in CIS and negative values indicate regions where the upward fluxes at the TOA are larger in CMIP3 than in CIS. Components of the radiative flux differences at the TOA were already discussed (cf. Fig. 11): over oceans the

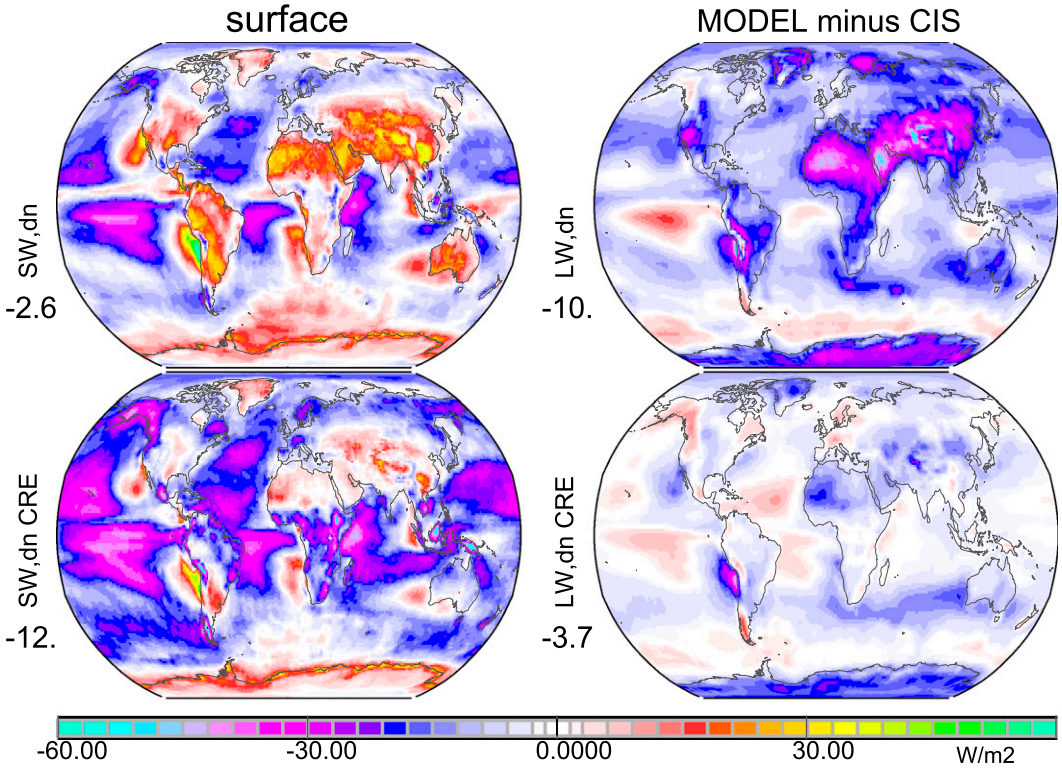

FIG. 12. As in Fig. 11, but at the surface for downward shortwave and downward longwave (cf. with Fig. 6 and Table 6). Note that downward fluxes are by definition positive (e.g., positive downward flux difference indicates a stronger downward flux in CMIP3 modeling and vice versa).

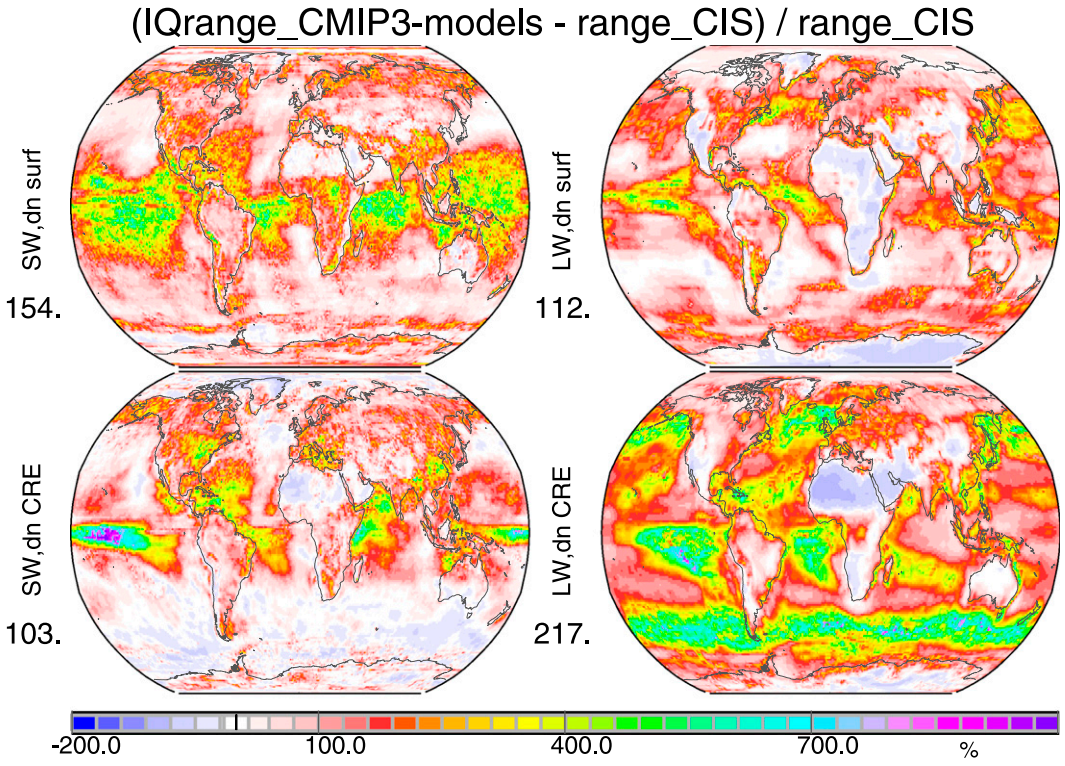

FIG. 13. Comparisons of spread ranges for downward (left) shortwave and (right) longwave radiative fluxes (top) during all-sky conditions and (bottom) contributing CRE. The local interquartile range in CMIP3 global modeling (ΔCMIP3) is compared with the local CIS range (ΔCIS) via the ratio of (ΔCMIP3 − ΔCIS) to (ΔCIS) in percent. Positive values indicate a larger diversity in the modeling. Negative values indicate a smaller diversity in the modeling. Values below the labels indicate global averages (%).

differences in the regional representation of the cloud radiative effects are mainly responsible for net flux difference patterns. Some net flux differences are reduced as local differences of SW CRE are partially compensated by (generally smaller) differences for LW CREs. Over the Sahara, differences seem to be related to weaker aerosol effects in climate modeling than in the observations.

The spatial features of the net flux differences at the surface in Fig. 14 show mainly negative values of different magnitudes as the surface net flux imbalance in CMIP3 is smaller than in CIS. Components of radiative net flux differences at the surface were already discussed (cf. Fig. 12). The strongest negative differences are over tropical and subtropical oceans outside the ITCZ, especially over the eastern Pacific. These differences (on the order of 30 $W m^{-2}$) are associated with cloud radiative effects in the trade wind cumulus regimes. Over continents, the differences from cloud effects are relatively small. Rare positive values occur over deserts (e.g., Sahara, Arabia, Australia) and are related to stronger clear-sky SW atmospheric transmission in climate modeling (aerosols).

Global averages of the local spreads, ΔCIS and ΔCMIP3, are compared in Tables 5–7. Also listed in those tables is (ΔCMIP3 − ΔCIS), shown in parentheses in Fig. 14. If the difference is positive, then the uncertainty in modeling (ΔCMIP3) is larger than in the observations. At the TOA, uncertainty differences are all strongly positive, demonstrating that the observational radiative flux products at the TOA qualify in general as a reference for climate modeling. At the surface, in contrast, the uncertainty differences are generally small and of both signs, indicating that the observational radiative flux products at the surface have lost their value as a reference for climate models, particularly because of the uncertainties in ancillary datasets. On the other hand, the patterns among the uncertainty differences suggest that the observational representation of cloud radiative effects is still useful for modeling comparison, especially over oceans.

Figure 15 compares local uncertainties of climate modeling, ΔCMIP3, with the observational uncertainties, ΔCIS, by showing the ratio [(ΔCMIP3 − ΔCIS)/ΔCIS]. Positive ratios indicate (as in Fig. 13) that observational data can serve as a reference for climate

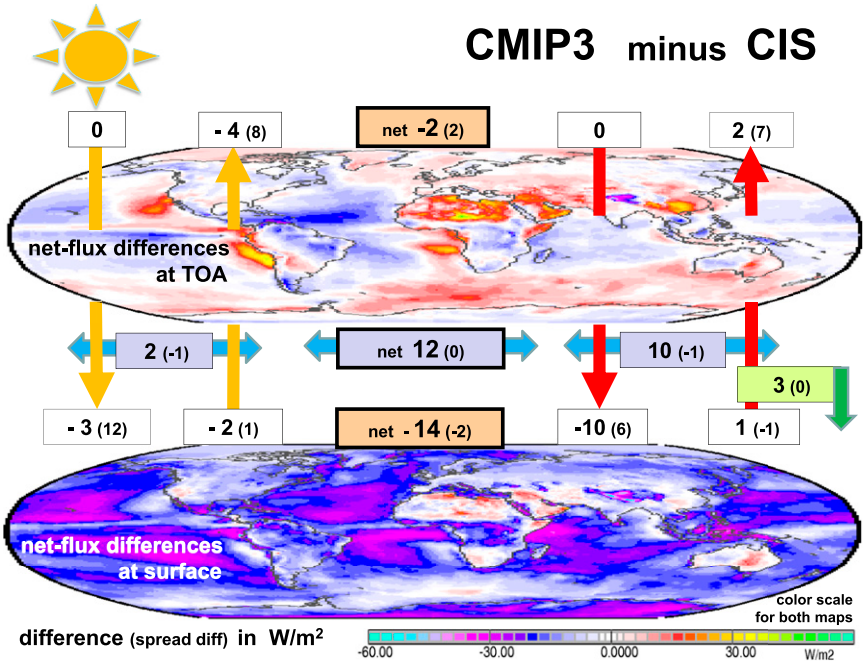

FIG. 14. Differences in multiyear annual averages for atmospheric SW and LW energy flows between CMIP3 and CIS. Globally averaged differences of the local uncertainties (ΔCMIP3 − ΔCIS) are given in parentheses. Compare with Fig. 9 for mean fluxes of CIS. The maps display CMIP3 − CIS differences for the net radiation at the TOA and Earth's surface.

modeling. At the TOA, the large ratios indicate that satellite datasets are a reliable reference, especially for the cloud effects at low and midlatitudes. Because of the uncertainties of ancillary data, however, the TOA net flux patterns over continents provide a more limited reference capability.

At the surface, the spread ratios are only positive over oceans but generally negative over continents. Thus, over many continental regions (e.g., northern Africa) the CIS net surface fluxes have lost their reference value to global climate modeling. The ratios for net flux uncertainties at the surface are more negative than those for the downward flux components, which were presented in Fig. 13. This indicates that it is the upward flux components (in particular the upward LW fluxes, which are directly dependent on ancillary data) that have increased the local spread in CIS over continents. More accurate and more consistent ancillary data than those currently used in the three satellite datasets are needed in order to qualify satellite data as a reference for climate modeling in those regions (cf. discussion in Zhang et al. 2007a).

e. *Atmospheric budgets*

Differences among the global averages and uncertainties of CMIP3 and CIS for the net atmospheric fluxes are compared in Table 7. Differences are presented for DIV, the separate contributing SW (warming) and LW (cooling) components, and the GH. In addition, clear-sky fluxes and CRE are provided.

TABLE 7. Comparisons of multiyear averages and averages of local spread (italics) for atmospheric radiative flux products of the entire atmosphere between typical values from satellite remote sensing (CIS and ΔCIS) and typical values from global modeling (CMIP3 and ΔCMIP3).

In the atmosphere ($W\,m^{-2}$)	SW + LW DIV			SW DIV			LW DIV			GH		
	All sky	Clear sky	CRE	All sky	Clear sky	CRE	All sky	Clear sky	CRE	All sky	Clear sky	CRE
CIS (2000–03)	−115	−111	−4	73	72	1	−188	−183	−5	154	127	27
CMIP3 (1984–95)	−103	−109	6	75	69	6	−178	−178	0	157	130	28
CMIP3 − CIS	12	2	10	2	−3	5	10	5	5	3	3	1
ΔCIS (2000–03)	*18*	*23*	*15*	*8*	*15*	*12*	*17*	*19*	*10*	*18*	*17*	*7*
ΔCMIP3 (1984–95)	*18*	*8*	*12*	*7*	*8*	*5*	*16*	*9*	*15*	*18*	*13*	*9*
ΔCMIP3 − ΔCIS	*0*	*−15*	*−3*	*−1*	*−7*	*−7*	*−1*	*−10*	*5*	*0*	*−4*	*2*

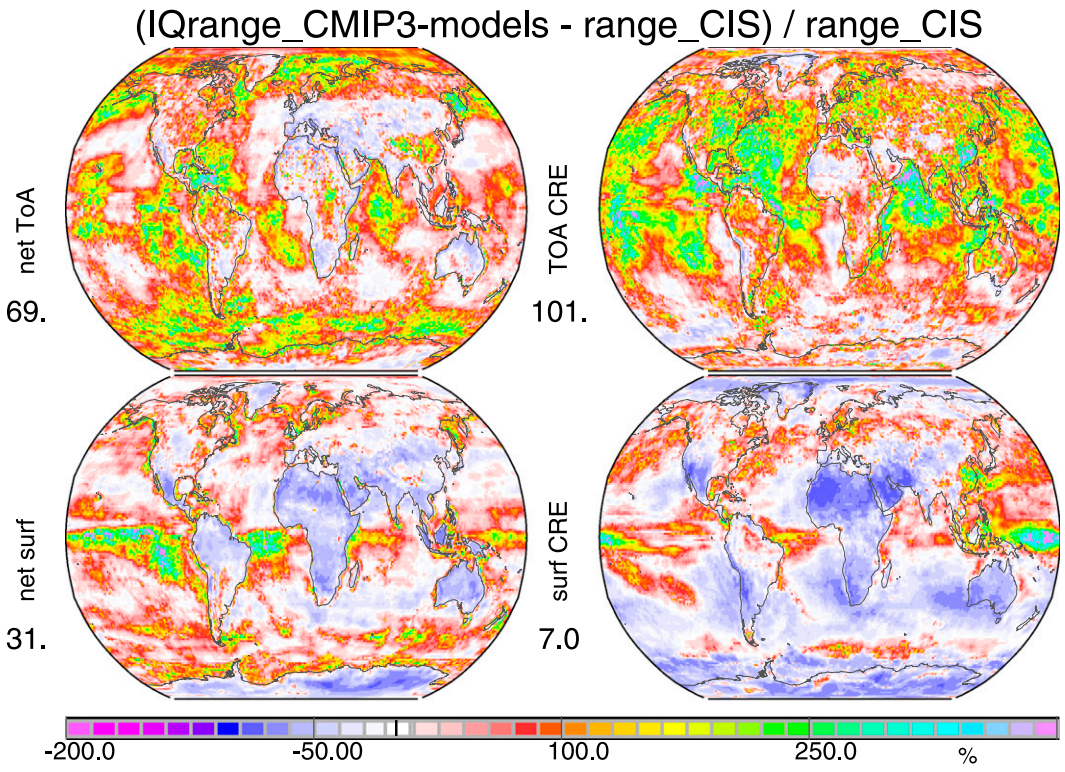

FIG. 15. Comparisons of uncertainties for (left) net fluxes at the TOA and surface and (right) contributing CRE. The local interquartile range in CMIP3 global modeling ΔCMIP3 is compared with the local CIS range ΔCIS via the ratio of (ΔCMIP3 − ΔCIS) to (ΔCIS) in percent. Positive values indicate a larger diversity in the CMIP3 modeling. Negative values indicate a smaller diversity in the CMIP3 modeling. Values below the labels indicate average ratios (%).

The net divergence in CMIP3 is less negative than for CIS (+12 W m^{-2}). Both SW (+2 W m^{-2} increased solar heating) and LW (+10 W m^{-2}, i.e., less LW cooling) components contribute. In CMIP3 larger SW warming by cloud absorption is partially compensated by weaker noncloud (aerosol) warming (as the aerosol radiative effects are weaker in climate modeling). The much smaller LW cooling in CMIP3 results equally from cloud and clear-sky contributions. The GH is slightly larger in the climate modeling than in the observational data.

Global averages of the local spreads of DIV and the GH are similar for observational data and climate modeling. However, the observational data have larger spreads in the separate contributions, especially for clear-sky divergence. Apparently, this clear-sky spread is compensated by the spread of the cloud effects. The smaller local spread in climate modeling for clear-sky DIV and the GH indirectly confirms an ancillary data problem for at least one of the satellite datasets.

Figure 16 details the spatial distribution of the differences between climate modeling, CMIP3, and the observational data, CIS, for DIV and the GH and the cloud contributions to these differences. Over almost the entire globe the atmospheric cooling in climate modeling is less negative than in the observations. Almost all the larger differences are found over oceans (up to 30–40 W m^{-2}) with maxima over the stratocumulus regions, over midlatitude oceans, and over ocean regions with strong convection. The GH in climate modeling is larger over oceans, especially in the central tropics, but weaker over dry continental areas. This can be attributed to lower surface temperatures than are suggested by observational data.

f. Ocean versus land fluxes

Scaled (with respect to the insolation at the TOA) averages for selected flux components of CIS between oceanic (“ocean”) and nonoceanic (“land”) subregions are compared in Table 4, which also contains the corresponding scaled averages from CMIP3, where the marked larger differences are now addressed. At the TOA there are no large differences in annual averages. At the surface over oceans both SW and LW net fluxes are significantly smaller in climate modeling. Smaller ocean net SW fluxes can be traced back to larger

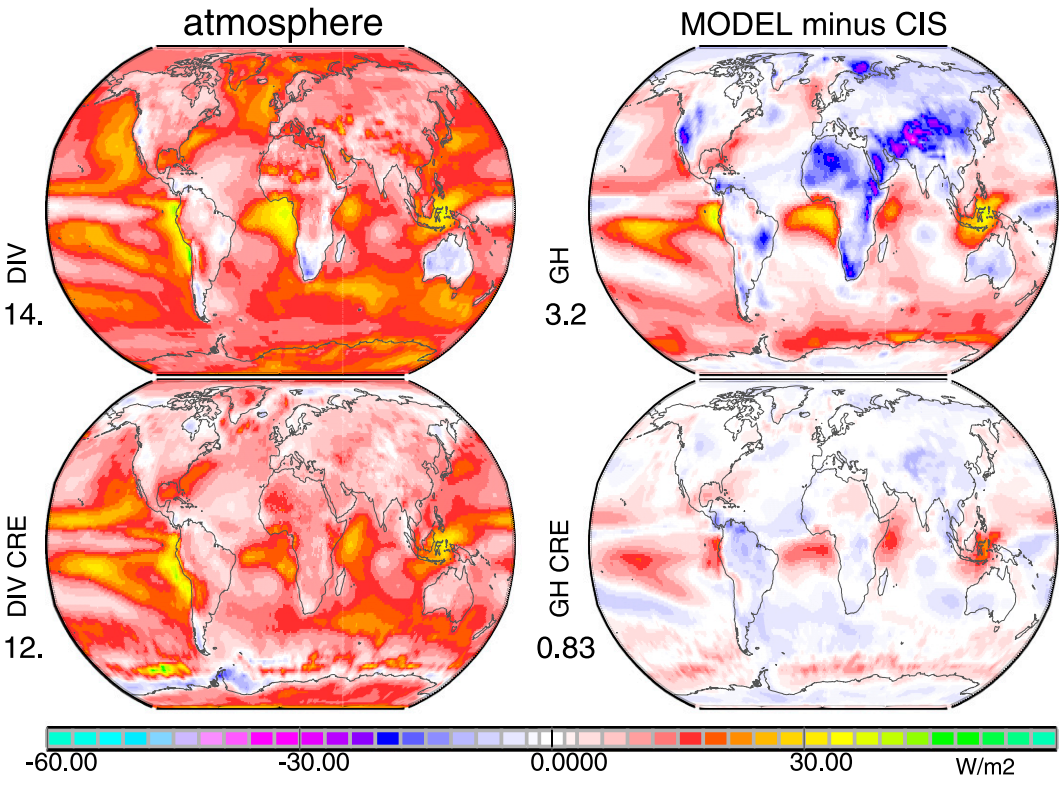

FIG. 16. Differences between central values from CMIP3 global modeling and CIS radiative fluxes (top) for the atmospheric net divergence and for the LW GH and (bottom) for associated CRE (cf. with Fig. 10). By definition divergence is negative and the GH is positive (e.g., a positive divergence difference indicates an underestimate in CMIP3 climate modeling).

downward SW flux reductions under cloudy conditions even though the downward SW fluxes under clear-sky conditions are slightly larger. Smaller oceanic net LW fluxes in climate modeling are mainly due to smaller downward LW fluxes that occur under clear-sky conditions. Reduced downward fluxes for both SW and LW under cloudy conditions could be explained by a combination of a larger cloud optical depth and a reduced cloud cover (which have different proportional effects in the SW and LW). Clear-sky differences of modeling can be explained in part by a smaller estimate of aerosol effects in climate modeling. At the surface over continents only the LW net fluxes are significantly smaller in climate modeling. Smaller downward fluxes in climate modeling are mainly associated with cloud-free conditions. Atmospheric divergence is significantly smaller in climate modeling over both ocean and land with the largest contributions from clouds over oceans.

4. Summary and conclusions

The time mean spatial distributions of the radiative energy flow for the Earth–atmosphere system from observational data products (CERES, ISCCP, and SRB) were compared to climate modeling outputs from CMIP3. The analysis focused on comparisons of characteristic averages and local spreads. For a better understanding of the spatial distribution patterns and local spreads, clear-sky fluxes and the contributions of clouds are also examined.

Characteristic observational data were defined by the local averages of CERES, ISCCP, and SRB, collectively called CIS, and the spread was quantified by the local range among CERES, ISCCP, and SRB, called ΔCIS. At the surface ΔCIS is larger than at TOA and larger over continents and higher latitudes than over oceans and lower latitudes. An examination of the contributions to ΔCIS by clouds and under cloud-free conditions indicated that the local spread for surface fluxes (and by definition for the atmosphere) is mostly caused by noncloud quantities. This was confirmed by the diagnosed local spread in ancillary data used to produce these products. This calls for more attention to and a review of all required ancillary data in terms of accuracy, stability, and temporal homogeneity.

Despite the ancillary data problems, the observational datasets offer valuable information on the temporal and spatial variability of radiative fluxes, especially those

TABLE 8. Comparison of multiyear global average radiative fluxes during all-sky conditions in the CIS dataset (boldface font), in the CMIP3 global climate modeling, and in four recent publications. Larger difference from CIS (>8 W m^{-2}) are highlighted for CMIP3 (italics) and for other publications (boldface italics).

All sky (W m^{-2})	CIS	CMIP3	Trenberth et al. (2011)	Stephens et al. (2012)	Wild et al. (2012)	L'Ecuyer et al. (2015)	L'Ecuyer et al. (2015)*
Total, net at TOA	**2**	0	0	0	0	0	0
SW, up at TOA	**−101**	−105	−102	−100	−100	−102	−102
LW, up at TOA	**−238**	−236	−239	−240	−239	−238	−238
SW, dn at surface	**190**	187	184	188	185	189	186
SW, up at surface	**−23**	−25	−23	−23	−24	−22	−22
LW, dn at surface	**344**	*334*	***333***	345	342	344	341
LW, up at surface	**−394**	−393	−396	−398	−397	−398	−399
SW, net at surface	**167**	162	161	165	161	167	164
LW, net at surface	**−50**	*−59*	***−63***	−53	−55	−54	***−58***
Total, net at surface	**117**	*103*	***98***	112	***105***	113	***106***
SW, DIV in atmosphere	**73**	75	79	75	79	71	74
LW, DIV in atmosphere	**−188**	*−178*	***−176***	−187	−184	−184	−180
Total, DIV in atmosphere	**−115**	*−103*	***−97***	−112	***−105***	−113	***−106***
IR GH at TOA	**154**	157	157	158	158	160	161

* Constrained to match known observations (e.g., 76 ± 6 W m^{-2} of GPCP precipitation data).

associated with cloud variations. Spatial distributions of annual averages were illustrated for important radiative flux components. Particularly useful are the more reliable (less contaminated by ancillary data) radiative fluxes at the TOA and the contributing spatial patterns of clouds. The consistency of the patterns and variation magnitude of the observed cloud radiative effects reveal characteristic biases in the representation of clouds in climate modeling, especially in their representation of lower-altitude clouds over oceans: cloud radiative effects in climate modeling are generally underestimated over stratocumulus regions but overestimated over trade wind cumulus regions.

A major difference between CIS and CMIP3 is in the net flux imbalance at the surface, especially over the oceans. Global averages are compared in Table 8. The CMIP3 net flux imbalance is 14 W m^{-2} smaller than for CIS. This raises the question of whether global modeling generally underestimates the latent heat release, surface evaporation, and precipitation. Table 8 also lists recent publications with alternate suggestions for the global average fluxes. The energy flow averages of Trenberth et al. (2011) also rely on the model interpretations of CMIP3, only their imbalance difference with CIS is even larger (−19 W m^{-2}). The more recent publications were aware of this surface net flux difference and tried to accommodate a larger downward LW flux that is closer to 345 W m^{-2}. These larger values were estimated with modified cloud properties by combining local statistics from passive and active remote sensing (Kato et al. 2013). Stephens et al. (2012) tried to accommodate CIS estimates by allowing larger error margins for all flux products. Their surface net flux imbalance difference with CIS was reduced to −3 W m^{-2} at the expense of larger contributions from sensible and especially latent heat. Their suggested larger latent heat release, however, was inconsistent with GPCP precipitation estimates (Adler et al. 2012; Huffman et al. 2009). Wild et al. (2012) tried a new energy flow estimate by scaling the surface fluxes of CMIP5 outputs to measured downward SW and LW radiative fluxes at BSRN surface sites. Their surface net flux imbalance difference with CIS was still −10 W m^{-2}. This is essentially the same difference when using the older CMIP3 global model output (Wild 2008). Within that context the energy flows in climate modeling output did not change significantly between CMIP3 and CMIP5 (Li et al. 2013). In a more recent energy flow estimate, L'Ecuyer et al. (2015) combined multiple information sources from satellite remote sensing and data assimilations, which not only addressed radiation, but also the best estimates for turbulent fluxes and precipitation. Their approach yielded good agreement with CIS, indicating a larger surface net flux imbalance and associated patterns of larger deviations over oceans compared to climate modeling. However, since their approach did not consider individual dataset uncertainties, in an alternate approach energy flows were reconstructed by considering uncertainties in the underlying energy and water budgets. Interestingly, the adjusted energy flow values are close to those of Wild et al. (2012) and consistent with satellite estimates for precipitation, again at the expense of a surface net flux imbalance, which is now again 9 W m^{-2} (on average) smaller than CIS.

The CIS surface net flux imbalance, which disagrees with satellite observations of precipitation, however,

could be in error. The surface fluxes of the so-called observational data are based on calculations that must make some assumptions or use other observational analyses for atmospheric properties (i.e., clouds, aerosol, water vapor, temperature). Most surface net flux differences between CIS and climate modeling occur over lower-latitude ocean areas, where constraints by surface reference data are poor or absent.

To obtain detailed but global information about surface energy flows, satellite-based products are necessary but more and better surface monitoring fluxes [e.g., BSRN-like NOAA buoys and the Marine Aerosol Network (MAN) of AERONET (http://aeronet.gsfc.nasa.gov/)] are needed, especially over oceans, to identify problems with these radiative flux calculations. These surface measurements have to combine both radiative flux measurements with measurements of the corresponding atmospheric (particularly clouds and aerosols) and surface conditions. The latter has to include more information about the site representativeness (vegetative cover and topography) of the measurements. Also, better (more accurate and more detailed space–time variations) information about what we have called ancillary properties of the atmosphere and surface is needed. The improvement of these global radiative flux products is required to support the improvements in climate model representations of cloud, atmospheric, and surface properties and their variations.

Acknowledgments. In the process of preparations for this contribution the authors gratefully acknowledged valuable discussions and suggestions made by many scientists, including Ellsworth Dutton, Laura Hinkelman, Seji Kato, Greg Kopp, Norman Loeb, Chuck Long, Atsumu Ohmura, George L. Smith, Tak-Meng Wong, and Yuan-C. Zhang. They also contributed with subchapters to the overarching GEWEX Radiation Flux Assessment Report. Stephan Bakan provided highly valuable comments during all phases of this paper. We also thank the two unknown reviewers for their constructive comments.

REFERENCES

Adler, R. F., G. Gu, and G. J. Huffman, 2012: Estimating climatological bias errors for the Global Precipitation Climatology Project (GPCP). *J. Appl. Meteor. Climatol.*, **51**, 84–99, doi:10.1175/JAMC-D-11-052.

Barkstrom, B. R., 1984: The Earth Radiation Budget Experiment (ERBE). *Bull. Amer. Meteor. Soc.*, **65**, 1170–1185, doi:10.1175/1520-0477(1984)065<1170:TERBE>2.0.CO;2.

Berger, A., 1978: Long-term variations of daily insolation and quaternary climate changes. *J. Atmos. Sci.*, **35**, 2362–2367, doi:10.1175/1520-0469(1978)035<2362:LTVODI>2.0.CO;2.

Doelling, D. R., D. F. Keyes, D. F. Young, B. A. Wielicki, and T. Wong, 2006: The newly released 5-year *Terra*-based monthly CERES radiative flux and cloud product. Preprints, *12th Conf. on Atmospheric Radiation*, Madison, WI, Amer. Meteor. Soc., 9.4. [Available online at https://ams.confex.com/ams/pdfpapers/112727.pdf.]

Dutton, E. G., J. J. Michalsky, T. Stoffel, B. W. Forgan, J. Hickey, D. W. Nelson, T. L. Alberta, and I. Reda, 2001: Measurement of broadband diffuse solar irradiance using current commercial instrumentation with a correction for thermal offset errors. *J. Atmos. Oceanic Technol.*, **18**, 297–314, doi:10.1175/1520-0426(2001)018<0297:MOBDSI>2.0.CO;2.

Duvel, J. P., and Coauthors, 2001: The ScaRaB–Resurs Earth radiation budget dataset and first results. *Bull. Amer. Meteor. Soc.*, **82**, 1397–1408, doi:10.1175/1520-0477(2001)082<1397:TSRERB>2.3.CO;2.

Gates, W. L., and Coauthors, 1999: An overview of the results of the Atmospheric Model Intercomparison Project (AMIP). *Bull. Amer. Meteor. Soc.*, **80**, 29–55, doi:10.1175/1520-0477(1999)080<0029:AOOTRO>2.0.CO;2.

Gruber, A., and V. Levizzani, 2008: Assessment of global precipitation products. WMO Rep. WCRP-128, WMP/TD 1430, 50 pp.

Gupta, S. K., N. A. Ritchey, A. C. Wilber, C. H. Whitlock, G. G. Gibson, and J. P. W. Stackhouse, 1999: A climatology of surface radiation budget derived from satellite data. *J. Climate*, **12**, 2691–2710, doi:10.1175/1520-0442(1999)012<2691:ACOSRB>2.0.CO;2.

——, P. W. Stackhouse Jr., S. J. Cox, J. C. Mikovitz, and T. Zhang, 2006: Surface radiation budget project completes 22-year data set. *GEWEX News*, Vol. 16, No. 4, Int. GEWEX Project Office, Silver Spring, MD, 12–13.

Hakuba, M. Z., D. Folloni, A. Sanchez-Lorenzo, M. Wild, 2013: Spatial representativeness of ground-based solar radiation measurements. *J. Geophys. Res.*, **118**, 8585–8597, doi:10.1002/jgrd.50673.

Harries, J. E., and Coauthors, 2005: The geostationary Earth Radiation Budget Experiment. *Bull. Amer. Meteor. Soc.*, **86**, 945–960, doi:10.1175/BAMS-86-7-945.

House, F. B., A. Gruber, G. E. Hunt, and A. T. Mecherikunnel, 1986: History of satellite missions and measurements of the Earth radiation budget (1957-1984). *Rev. Geophys.*, **24**, 357–377, doi:10.1029/RG024i002p00357.

Huffman, G. J., R. F. Adler, D. T. Bolvin, and G. Gu, 2009: Improving the global precipitation record: GPCP version 2.1. *Geophys. Res. Lett.*, **36**, L17808, doi:10.1029/2009GL040000.

IPCC, 2007: *Climate Change 2007: The Physical Science Basis*. Cambridge University Press, 996 pp.

Kato, S., N. Loeb, D. Rutan, F. Rose, S. Mack, W. Miller, and Y. Chen, 2012: Uncertainty estimate of surface irradiances computed with MODIS-, *CALIPSO*-, and *CloudSat*-derived cloud and aerosol properties. *Surv. Geophys.*, **33**, 395–412, doi:10.1007/s10712-012-9179-x.

——, ——, F. G. Rose, D. R. Doelling, D. A. Rutan, T. E. Caldwell, L. Yu, and R. A. Weller, 2013: Surface irradiances consistent with CERES-derived top-of-atmosphere shortwave and longwave irradiances. *J. Climate*, **26**, 2719–2740, doi:10.1175/JCLI-D-12-00436.1.

Kopp, G., and J. Lean, 2011: A new, lower value of total solar irradiance: Evidence and climate significance. *Geophys. Res. Lett.*, **38**, L01706, doi:10.1029/2010GL045777.

L'Ecuyer, T., and Coauthors, 2015: The observed state of the energy budget in the early twenty-first century. *J. Climate*, **28**, 8319–8346, doi:10.1175/JCLI-D-14-00556.1.

Lee, R. B., III, M. A. Gibson, N. Shivakumar, R. Wilson, H. L. Kyle, and A. T. Mecherikunnel, 1991: Solar irradiance measurements: Minimum through maximum solar activity. *Meteorologia*, **28**, 265–268, doi:10.1088/0026-1394/28/3/032.

Li, J., B. E. Carlson, and A. A. Lacis, 2009: A study on the temporal and spatial variability of absorbing aerosols using Total Ozone Mapping Spectrometer and Ozone Monitoring Instrument Aerosol Index data. *J. Geophys. Res.*, **114**, D09213, doi:10.1029/2008JD011278.

Li, J.-L. F., D. E. Waliser, G. Stephens, S. Lee, T. I. Ecuyer, S. Kato, N. Loeb, and H.-Y. Ma, 2013: Characterizing and understanding radiation budget biases in CMIP3/CMIP5 GCMs, contemporary GCM and reanalysis. *J. Geophys. Res. Atmos.*, **118**, 8166–8184, doi:10.1002/jgrd.50378.

Loeb, N. G., K. J. Priestley, D. P. Kratz, E. B. Geier, R. N. Green, B. Wielicki, and S. K. Nolan, 2001: Determination of unfiltered radiances from the Clouds and the Earth's Radiation Energy System instrument. *J. Appl. Meteor.*, **40**, 822–835, doi:10.1175/1520-0450(2001)040<0822:DOURFT>2.0.CO;2.

——, B. A. Wielicki, D. R. Doelling, G. L. Smith, D. F. Keyes, S. Kato, N. M. Smith, and T. Wong, 2009: Toward optimal closure of the earth's top-of-atmosphere radiation budget. *J. Climate*, **22**, 748–766, doi:10.1175/2008JCLI2637.1.

Long, C. N., and D. D. Turner, 2008: A method for continuous estimation of clear-sky downwelling longwave radiative flux developed using ARM surface measurements. *J. Geophys. Res.*, **113**, D18206, doi:10.1029/2008JD009936.

Neckel, H., and D. Labs, 1984: The solar radiation between 3300 and 12500A. *Solar Phys.*, **90**, 205–258, doi:10.1007/BF00173953.

Ohmura, A., and Coauthors, 1998: Baseline Surface Radiation Network: New precision radiometry for climate research. *Bull. Amer. Meteor. Soc.*, **79**, 2115–2136, doi:10.1175/1520-0477(1998)079<2115:BSRNBW>2.0.CO;2.

Ohring, G., B. Wielicki, R. Spencer, B. Emery, and R. Datla, 2005: Satellite instrument calibration for measuring global climate change. *Bull. Amer. Meteor. Soc.*, **86**, 1303–1313, doi:10.1175/BAMS-86-9-1303.

Oreopoulos, L., and Coauthors, 2012: The Continual Intercomparison of Radiation Codes: Results from Phase I. *J. Geophys. Res.*, **117**, D06118, doi:10.1029/2011JD016821.

Raschke, E., T. H. Vonder Haar, W. R. Bandeen, and M. Pasternak, 1973: The annual radiation budget of the Earth-atmosphere system during 1969–70 from *Nimbus 3* measurements. *J. Atmos. Sci.*, **30**, 341–364, doi:10.1175/1520-0469(1973)030<0341:TARBOT>2.0.CO;2.

——, M. A. Giorgetta, S. Kinne, and M. Wild, 2005: How accurate did GCMs compute the insolation at TOA for AMIP-2? *Geophys. Res. Lett.*, **32**, L23707, doi:10.1029/2005GL024411.

——, S. Kinne, and P. W. Stackhouse Jr., 2012a: GEWEX Radiative Flux Assessment (RFA) Volume 1: Assessment. WCRP Rep. 19/2012, 273 pp. [Available online at http://www.wcrp-climate.org/documents/GEWEX%20RFA-Volume%201-report.pdf.] Vol. 1: Scientific Results, 520 pp, Vol. 2: Appendices and Details, 500 pp.

——, ——, and ——, 2012b: GEWEX Radiative Flux Assessment (RFA) Volume 2: Appendices with supplementary information. WCRP Rep. 19/2012, 215 pp.

Roesch, A., M. Wild, A. Ohmura, E. Dutton, C. N. Long, and T. Zhang, 2011: Assessment of the completeness of BSRN radiation records and the consequence for the computation of monthly means. *Atmos. Meas. Tech.*, **4**, 339–354, doi:10.5194/amt-4-339-2011.

Rossow, W. B., and A. A. Lacis, 1990: Global, seasonal cloud variations from satellite radiance measurements. Part II: Cloud properties and radiative effects. *J. Climate*, **3**, 1204–1253, doi:10.1175/1520-0442(1990)003<1204:GSCVFS>2.0.CO;2.

——, and R. Schiffer, 1999: Advances in understanding clouds from ISCCP. *Bull. Amer. Meteor. Soc.*, **80**, 2261–2287, doi:10.1175/1520-0477(1999)080<2261:AIUCFI>2.0.CO;2.

Smith, G. L., R. N. Green, E. Raschke, L. M. Avis, J. T. Suttles, B. A. Wielicki, and R. Davies, 1986: Inversion methods for satellite studies of the earth's radiation budget: Development of algorithms for the ERBE mission. *Rev. Geophys.*, **24**, 407–421, doi:10.1029/RG024i002p00407.

——, Z. P. Szewczyk, D. A. Rutan, and R. B. Lee, 2006: Comparison of measurements from satellite radiation budget instruments. *J. Geophys. Res.*, **111**, D04101, doi:10.1029/2005JD006307.

Stackhouse, P. W., S. J. Cox, S. Gupta, M. Chiacchio, and J. C. Mikovitz, 2001: The WCRP / GEWEX surface radiation budget project release 2: An assessment of surface fluxes at 1degree resolution. *IRS 2000, Current Problems in Atmospheric Radiation*, W. Smith and Y. Timofeyev, Eds. A. Deepak Publishing, 485–488.

——, S. K. Gupta, S. J. Cox, T. Zhang, J. C. Mikovitz, and L. M. Hinkelman, 2011: The NASA/GEWEX Surface Radiation Budget Release 3.0: 24.5-Year dataset. *GEWEX News*, Int. GEWEX Project Office, Silver Spring, MD, 10–12. [Available online at http://www.gewex.org/gewex-content/files_mf/1432209318Feb2011.pdf.]

Stephens, G. L., and Coauthors, 2002: The *CloudSat* mission and the A-Train: A new dimension of space-based observations of clouds and precipitation. *Bull. Amer. Meteor. Soc.*, **83**, 1771–1790, doi:10.1175/BAMS-83-12-1771.

——, and Coauthors, 2012: An update on the earth's energy balance in light of the latest global observation. *Nat. Geosci.*, **5**, 691–696, doi:10.1038/ngeo1580.

Stubenrauch, C. J., and Coauthors, 2013: Assessment of global cloud datasets from satellites: Project and database initiated by the GEWEX Radiation Panel. *Bull. Amer. Meteor. Soc.*, **94**, 1031–1049, doi:10.1175/BAMS-D-12-00117.1.

Trenberth, K. E., J. T. Fasullo, and J. Mackaro, 2011: Atmospheric moisture transports from ocean to land and global energy flows in reanalysis. *J. Climate*, **24**, 4907–4924, doi:10.1175/2011JCLI4171.1.

Wielicki, B. W., R. D. Cess, M. D. King, D. A. Randall, and E. F. Harrison, 1995: Mission to Planet Earth: Role of clouds and radiation in climate. *Bull. Amer. Meteor. Soc.*, **76**, 2125–2153, doi:10.1175/1520-0477(1995)076<2125:MTPERO>2.0.CO;2.

——, B. R. Barkstrom, E. F. Harrison, R. B. Lee III, G. L. Smith, and J. E. Cooper, 1996: Clouds and the Earth's Radiant Energy System (CERES): An Earth Observing System experiment. *Bull. Amer. Meteor. Soc.*, **77**, 853–868, doi:10.1175/1520-0477(1996)077<0853:CATERE>2.0.CO;2.

Wild, M., 2008: Short-wave and long-wave surface radiation budgets in GCMs: A review based on the IPCC-AR4/CMIP3 models. *Tellus*, **60A**, 932–945, doi:10.1111/j.1600-0870.2008.00342.x.

——, B. Trüssel, A. Ohmura, C. N. Long, G. König-Langlo, E. G. Dutton, and A. Tvetskov, 2009: Global dimming and brightening: An update beyond 2000. *J. Geophys. Res. Atmos.*, **114**, D00D13, doi:10.1029/2008JD011382.

——, D. Folini, Ch. Schär, N. Loeb, E. G. Dutton, and G. König-Langlo, 2012: The global energy balance from a surface

perspective. *Climate Dyn.*, **40**, 3107–3134, doi:10.1007/s00382-012-1569-8.

Zhang, Y.-C., and W. B. Rossow, 1997: Estimating meridional energy transports by the atmospheric and oceanic general circulation using boundary flux data. *J. Climate*, **10**, 2358–2373, doi:10.1175/1520-0442(1997)010<2358:EMETBT>2.0.CO;2.

——, ——, and A. A. Lacis, 1995: Calculation of surface and top-of-atmosphere radiative fluxes from physical quantities based on ISCCP datasets, Part I: Method and sensitivity to input data uncertainties. *J. Geophys. Res.*, **100**, 1149–1165, doi:10.1029/94JD02747.

——, ——, ——, V. Oinas, and M. I. Mishchenko, 2004: Calculation of radiative fluxes from the surface to top of atmosphere based on ISCCP and other global data sets: Refinements of the radiative transfer model and the input data. *J. Geophys. Res.*, **109**, D19105, doi:10.1029/2003JD004457.

——, ——, and P. W. Stackhouse, 2006: Comparison of different global information sources used in surface radiative flux calculation: Radiative properties of the near-surface atmosphere. *J. Geophys. Res.*, **111**, D13106, doi:10.1029/2005JD006873.

——, ——, and ——, 2007a: Comparison of different global information sources used in surface radiative flux calculation: Radiative properties of the surface. *J. Geophys. Res.*, **112**, D01102, doi:10.1029/2005JD007008.

——, ——, ——, A. Romanou, and B. A. Wielicki, 2007b: Decadal variations of global energy and ocean heat budget and meridional energy transports inferred from recent global data sets. *J. Geophys. Res.*, **112**, D22101, doi:10.1029/2007JD008435.

——, ——, C. N. Long, and E. G. Dutton, 2010: Exploiting diurnal variations to evaluate the ISCCP-FD flux calculations and Radiative-Flux-Analysis-Processed Surface Observations from BSRN, ARM, and SURFRAD. *J. Geophys. Res.*, **115**, D15105, doi:10.1029/2009JD012743.